

## 1. Outline of Meteorological Satellite Observation

### 1.1. Observation by Meteorological Satellites

An advantage of meteorological satellite-based observation is the capacity for consistent worldwide monitoring with high spatial resolution. It enables monitoring of short-term atmospheric phenomena such as the development of cumulonimbus masses, cloud areas in lows/typhoons, and climate change.

#### 1.1.1. Satellite Orbit

The major satellite orbits used in meteorological observation are geostationary and polar sun-synchronous. Geostationary satellites follow the earth's rotation over the equator, making them appear stationary from the earth. These include JMA's Himawari-8/9 units orbiting at 140.7°E at altitudes of approximately 35,800 km, with observation of the area from the North Pole to the South Pole at intervals of around 10 minutes for monitoring of weather disturbances and climate change. Polar-orbiting satellites observe 2,000 – 3,000 km widths across the orbit in latitudinal circulation at relatively low altitudes in short cycles (e.g., around 850 km high with 100 minutes per cycle in the NOAA series). Low-orbit observation provides higher-resolution imagery than that of geostationary satellites, but covers the same position in the sky only twice a day.

#### 1.1.2. Observation by Himawari-8/9

Himawari-8/9 observe using a moving internal mirror that scans the earth longitudinally from the north in a stepwise fashion (Bessho et al. 2016). The figure below illustrates Himawari-8/9's complete full-disk observation (i.e., covering the entire earth as seen from the satellite) and five area observations. Himawari-8/9 observation is based on observation timeline with a basic interval of 10 minutes. The figure shows the observation areas and frequencies on a timeline of 10 minutes.

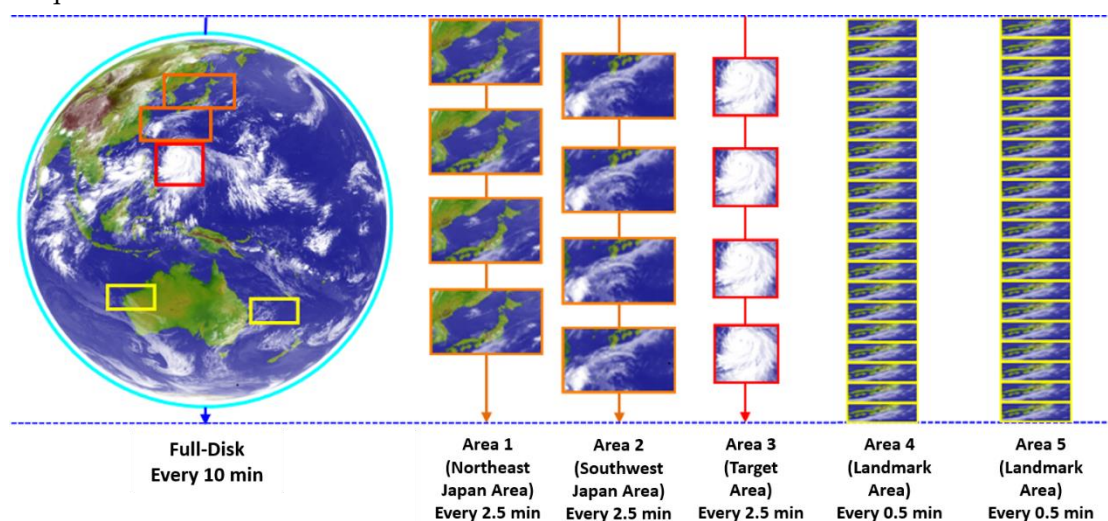


Fig. 1-1-1. Himawari-8/9 observation areas and frequencies on a timeline of 10 minutes

Himawari-8/9 perform a full-disk observation and five area observations on the timeline of 10 minutes. Two observations (i.e., 2,000-km longitudinal and 1,000-km latitudinal, as per the orange rectangles in Fig. 1-1-1) are made every 2.5 minutes over the area around Japan. These two areas are fixed, while the area in the red rectangle for typhoon monitoring (1,000-km longitudinal and latitudinal) can be changed every 2.5 minutes for specific focus on typhoons, cyclones and volcanic eruptions. In two other areas (1,000-km longitudinal, 500-km latitudinal), locations for observation can be changed every 30 seconds. This produces imagery relating to coastline characteristics as landmarks to enable correction of satellite attitude parameters based on positional differences between landmarks and predictions. The 30-second frequency of imagery capture allows monitoring of rapidly developing cumulonimbus areas that may cause extreme phenomena.

Wavelength (μm)	Himawari-8/9				Himawari-6/7		Example usages
	Band no.	Horizontal resolution (km)	Central wavelength (μm)		Channe 1	Horizontal resolution (km)	
			Himawari -8	Himawari -9			
0.47	1	1	0.47	0.47		-	Color composite imagery, aerosols
0.51	2	1	0.51	0.51	-	-	Color composite imagery, aerosols
0.64	3	0.5	0.64	0.64	VIS	1	Color composite imagery, low cloud/fog
0.86	4	1	0.86	0.86			Vegetation, aerosols
1.6	5	2	1.61	1.61			Discrimination of cloud phases
2.3	6	2	2.26	2.26			Cloud particle radius variation
3.9	7	2	3.89	3.83	IR4	4	Low cloud/fog, natural fires
6.2	8	2	6.24	6.25	IR3	4	Upper-layer water vapor concentration
6.9	9	2	6.94	6.96			Middle-layer water vapor concentration
7,3	10	2	7.35	7.34			Middle-layer water vapor concentration
8.6	11	2	8.59	8.59			Discrimination of cloud phases, SO <sub>2</sub>
9.6	12	2	9.64	9.63			Ozone total volume
10.4	13	2	10.41	10.41	IR1	4	Cloud imagery, cloud-top information
11.2	14	2	11.24	11.21			Cloud imagery, sea surface temperature
12.4	15	2	12.38	12.36	IR2	4	Cloud imagery, sea surface temperature
13.3	16	2	13.28	13.31			Cloud-top height

Table 1. Comparison of Himawari-8/9 and Himawari-6/7 bands. Spatial resolutions are as defined at the subsatellite point.

### 1.1.1. Advanced Himawari Imagers on board Himawari-8/9

The Advanced Himawari Imager (AHI) units on board the Himawari-8/9 satellites feature 16 bands (3 visible, 3 near-infrared and 10 infrared). Table 1 compares these bands with those on the previous Himawari-6/7 units, with the rightmost column showing example usages of observation data for each band. The characteristics of each band are detailed in the next section.

#### References:

- Bessho et al., 2016: An introduction to Himawari-8/9 - Japan's new-generation geostationary meteorological satellites. *J. Meteor. Soc. Japan*, 94, 151-183.  
<https://doi.org/10.1007/978-3-642-14791-3>

## 1.2. Himawari-8/9 AHI Band Characteristics

As described previously, the Advanced Himawari Imagers (AHIs) on Himawari-8/9 have 16 bands in the visible, near-infrared and infrared ranges, as opposed to the 5 bands of the Himawari-6 and 7 imagers. Difference imagery is also created with focus on solar reflectance and brightness temperature for each corresponding pixel. This section describes these bands along with difference imagery used in cloud analysis and RGB composite imagery.

### 1.2.1. Visible Imagery

#### (1) Introduction of Visible Imagery

Visible imagery shows solar reflectance (usually not corrected for solar zenith angle) in the wavelength range of visible light (roughly from 0.4 to 0.8  $\mu\text{m}$ ). Areas with strong solar reflection are rendered with bright pixels, highlighting dense clouds and snow. Sea surfaces have weak solar reflection, making them appear dark. Targets appear differently depending on solar elevation. As reflection energy is lower with incident energy per unit area, high-latitude regions appear darker than low-latitude regions, and images in the morning and evening are darker than those at noon. Some cloud areas are also darker due to the shade of vertically developed cumulonimbus. Figure 1-2-1 shows a lower cloud that became harder to see due to cumulonimbus shade. Areas without sunlight at night appear pitch black.

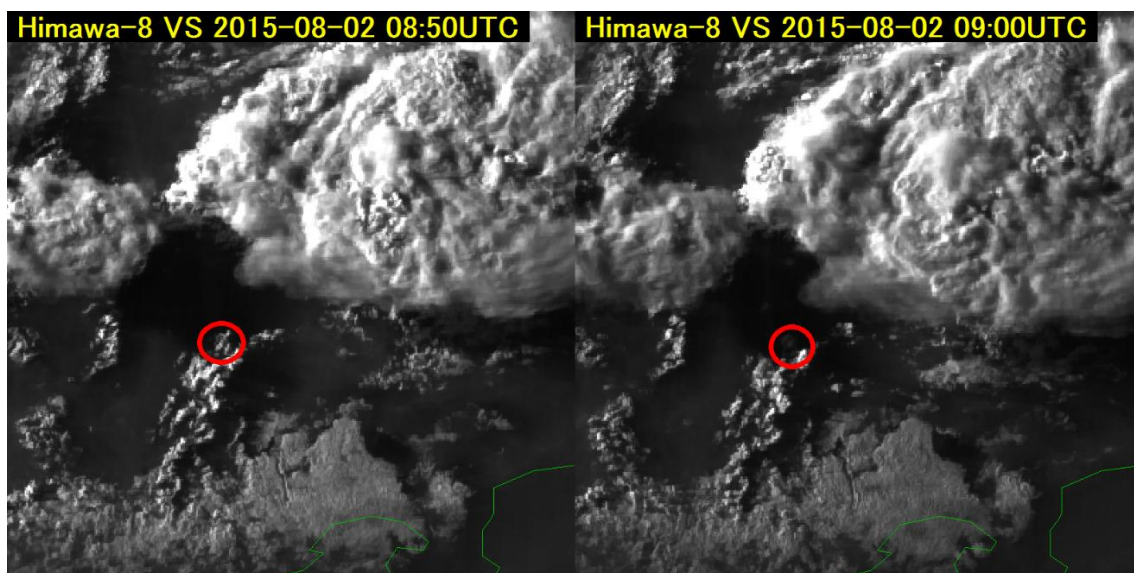


Fig. 1-2-1 Lower cloud entering the cumulonimbus shade

Himawari-6 and 7 had only a single band with a central wavelength of around 0.68  $\mu\text{m}$ , while Himawari-8/9 have three bands with central wavelengths of around 0.47, 0.51 and 0.64  $\mu\text{m}$ , corresponding to blue, green and red in human vision. These colors form True Color RGB composite imagery resembling the earth as viewed by the human eye from outer space.

Figure 1-2-2 shows solar reflection characteristics in visible and near-infrared ranges. Even within the visible range, these depend on wavelength (see Section 1.2.5).

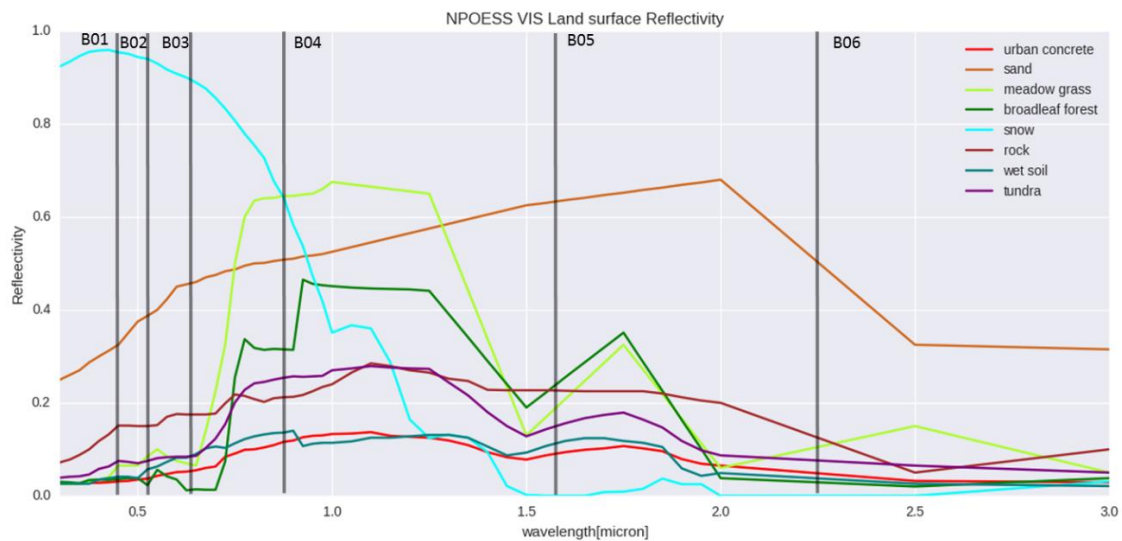


Fig. 1-2-2 Solar reflectance of land surface types in the Community Radiative Transfer Model (CRTM) in the visible and near-infrared ranges. The black lines indicate the central wavelengths of Himawari-8 AHI Bands 1 - 6.

## (2) Visible Imagery Usage

### A) Distinction between Thick and Thin Clouds

The solar reflectance of clouds depends on their density of particles, with lower clouds typically containing more particles and appearing brighter. Vertically developed thick clouds such as cumulonimbus also have a high particle count, making them appear bright. Thin upper clouds may be transparent, revealing the state of lower clouds and land/sea surfaces below.

### B) Distinction between Convective and Stratiform Clouds

The top surfaces of stratiform clouds are smooth and uniform, while those of convective clouds are rough and uneven. These textures are highlighted when sunlight hits at an angle.

### C) Cloud Top Height Comparison

When sunlight hits at an angle, clouds with a higher top may form shadows over those below. This allows comparison of top heights.

### D) Land Surface Identification

Figure 1-2-3 shows solar reflectance for individual land conditions in the visible range (from the same source as Fig. 1-2-2). Within the wavelengths of AHI Bands 1 – 3 in particular, snow

shows the largest reflectance, then sand, then vegetation (much smaller).

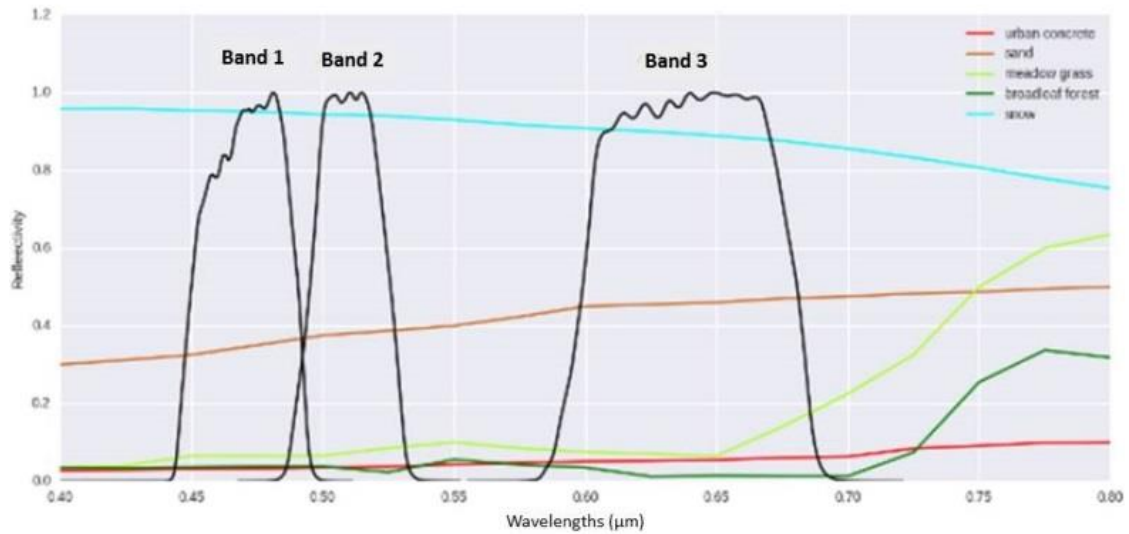


Fig. 1-2-3 Solar reflectance of land surface types in the CRTM in the visible range. Black lines indicate response functions of Himawari-8 AHI Bands 1 – 3.

As an example, the True Color RGB composite image in Fig. 1-2-4 shows desert areas in Australia. These appear reddish-brown because Bands 1 (blue) and 2 (green) contribute less than Band 3 (red), as shown by the sand characteristics in Fig. 1-2-3. Green is unrecognizable even in vegetation areas such as tropical rainforests.

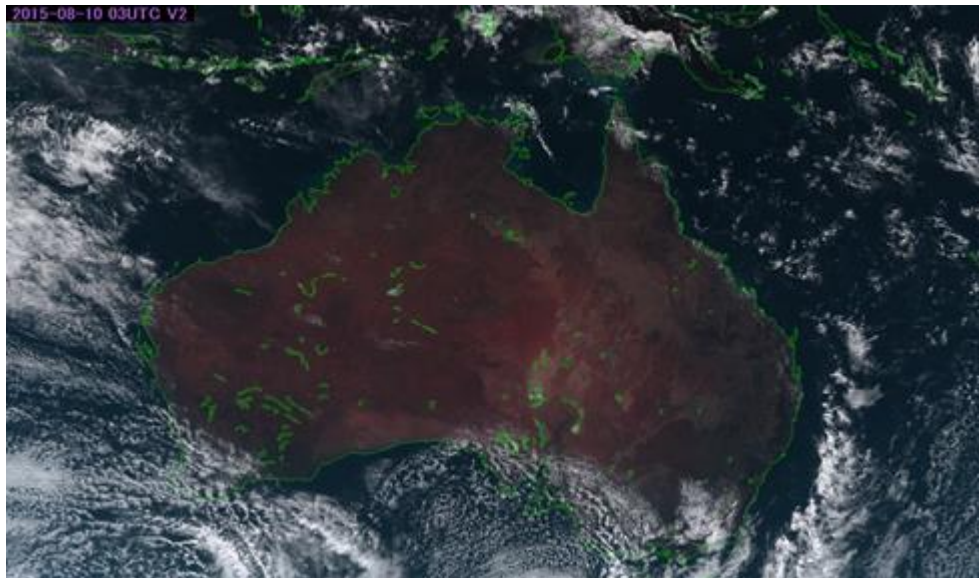


Fig. 1-2-4 True Color RGB composite image of Australia

#### E) Aerosol Identification

In Band 1, aerosol masses such as smoke and dust are clearly visible due to Mie scattering when the size of the scattering particles is comparable to the wavelength of the light. Figure 1-2-5 shows continental wildfire smoke over the Sea of Japan. This is clearer in Band 1 image

(with a shorter central wavelength) than in Band 3 image.

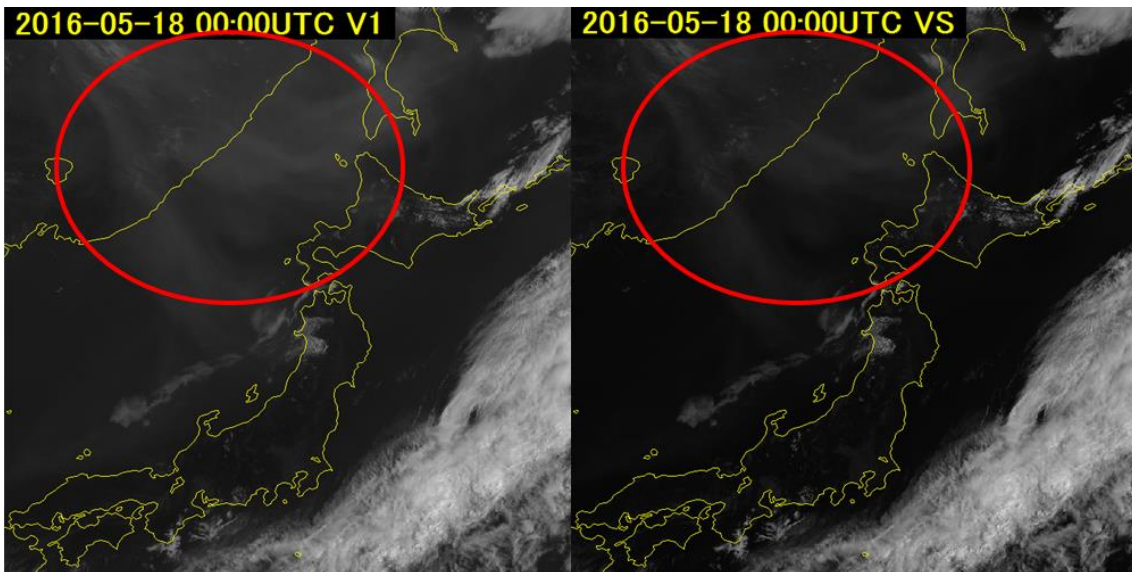


Fig. 1-2-5 Continental wildfire smoke over the Sea of Japan; more apparent in Band 1 (left) than in Band 3 (right)

1.2.2. Near-infrared Imagery

(1) Introduction

Himawari-8 is the first satellite in the Himawari series to have near-infrared bands, which are toward the longer-wavelength side of the visible range. Although invisible to the human eye, the range is widely used in everyday items such as optical fibers and remote controls.

Observed radiance in such imagery consists mostly of reflected sunlight, and radiation from the Earth in this can largely be ignored (as in visible imagery). Accordingly, the medium applies only to daytime conditions. However, it can reveal characteristic reflections that differ from those of visible bands, especially for land surfaces and ice clouds (Fig. 1-2-2).

(2) Usage

A) Land Surface Determination (All Bands)

As per Fig. 1-2-6, Band 4 shows large solar reflectances for vegetation such as grassland and broadleaf forest areas. It can also be used to identify burnt areas (which show smaller solar reflectance than healthy vegetation; Fig. 1-2-7), and renders coastlines more clearly than Band 3 (Fig. 1-2-8). Band 5 can be used to distinguish between lower-level water clouds and snow/ice-covered land because it shows much smaller solar reflectance values than Bands 1 to 4 (Fig. 1-2-2).

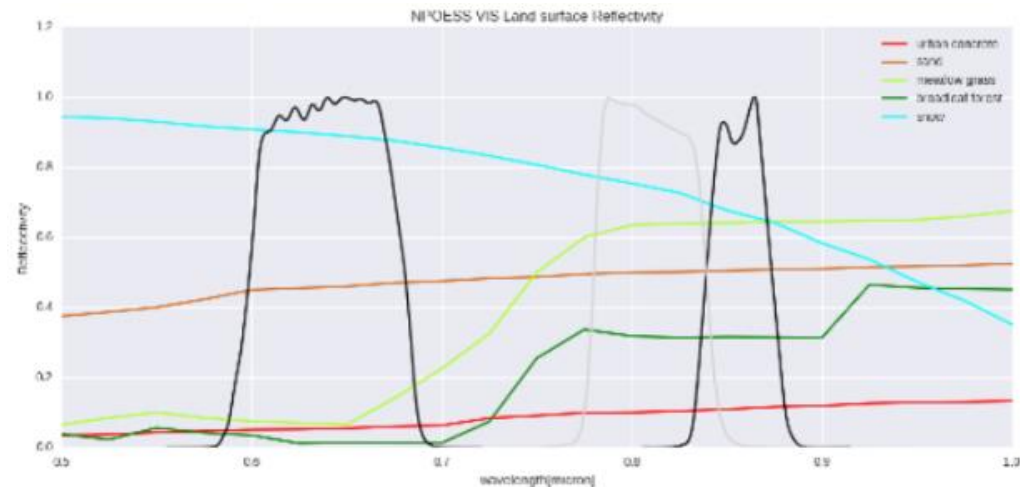


Fig. 1-2-6 Solar reflectances from 0.5 to 1.0 μm corresponding to land surfaces in CRTM (Delst and Han, 2008), with response functions of Himawari-8 AHI Bands 3 and 4 in black and MSG SEVIRI VIS0.8 in grey.

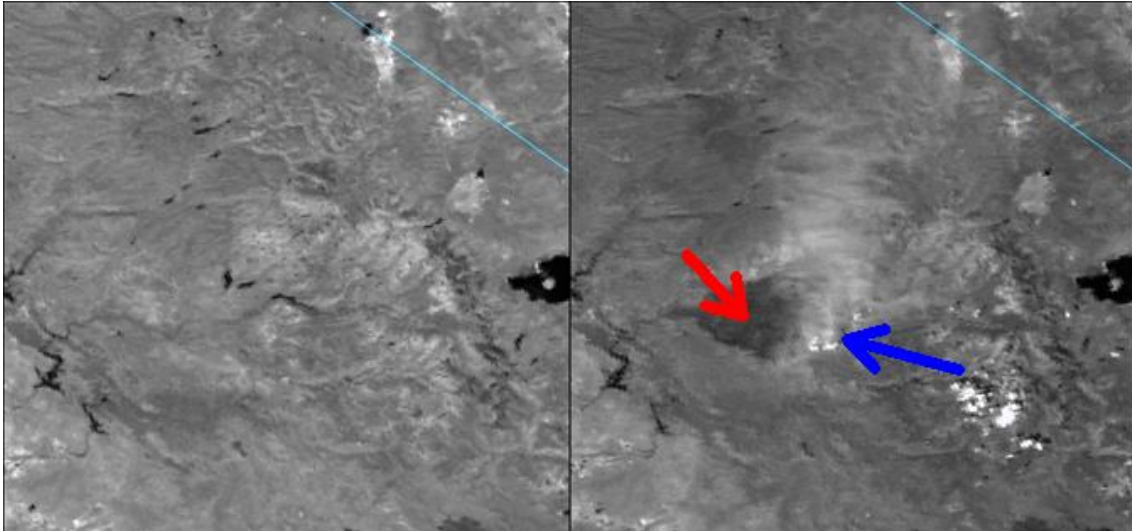


Fig. 1-2-7 M7 band image (0.865  $\mu\text{m}$ ) on S-NPP/VIIRS before (left) and after (right) a California wildfire. Red arrow: burnt area and smoke; blue arrow: thick pyro-cumulus associated with fire and volcanic activity (GOES-R Program Office, 2015).

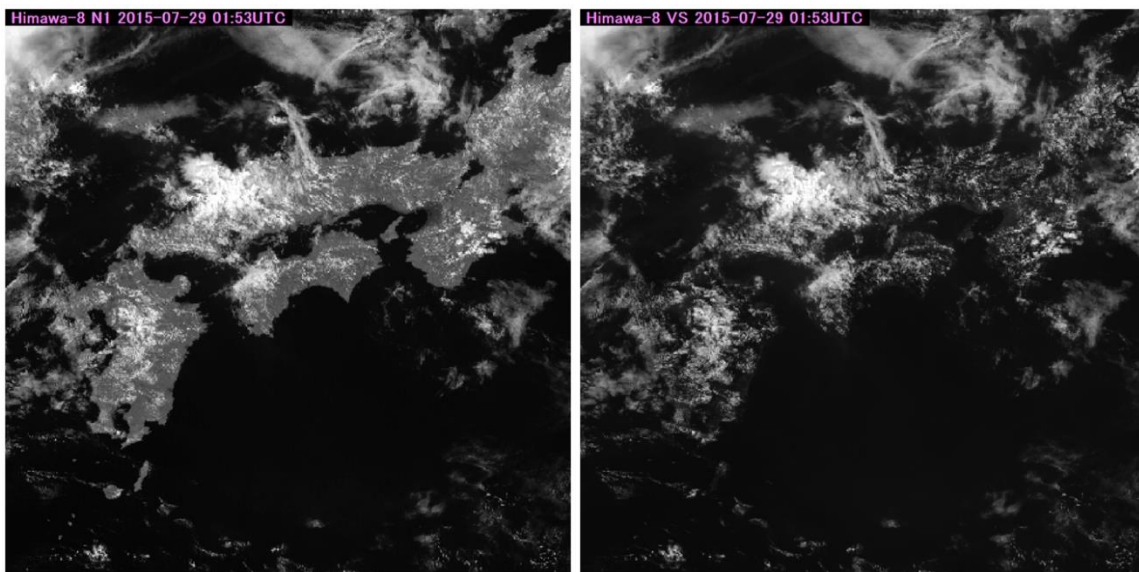


Fig. 1-2-8 Band 4 (left) and Band 3 (right) images. The coastlines in Band 4 are obviously clearer.

#### B) Cloud Particle Phase/Size Determination (Bands 5 and 6)

Solar reflectances in both bands vary by particle phase (i.e., water or ice) at the cloud top. When sunlight is perpendicularly incident from a medium with a refractive index  $n_1$  to one with  $n_2$ , reflectance  $R$  is expressed by:

$$R = \left( \frac{n_1 - n_2}{n_1 + n_2} \right)^2$$

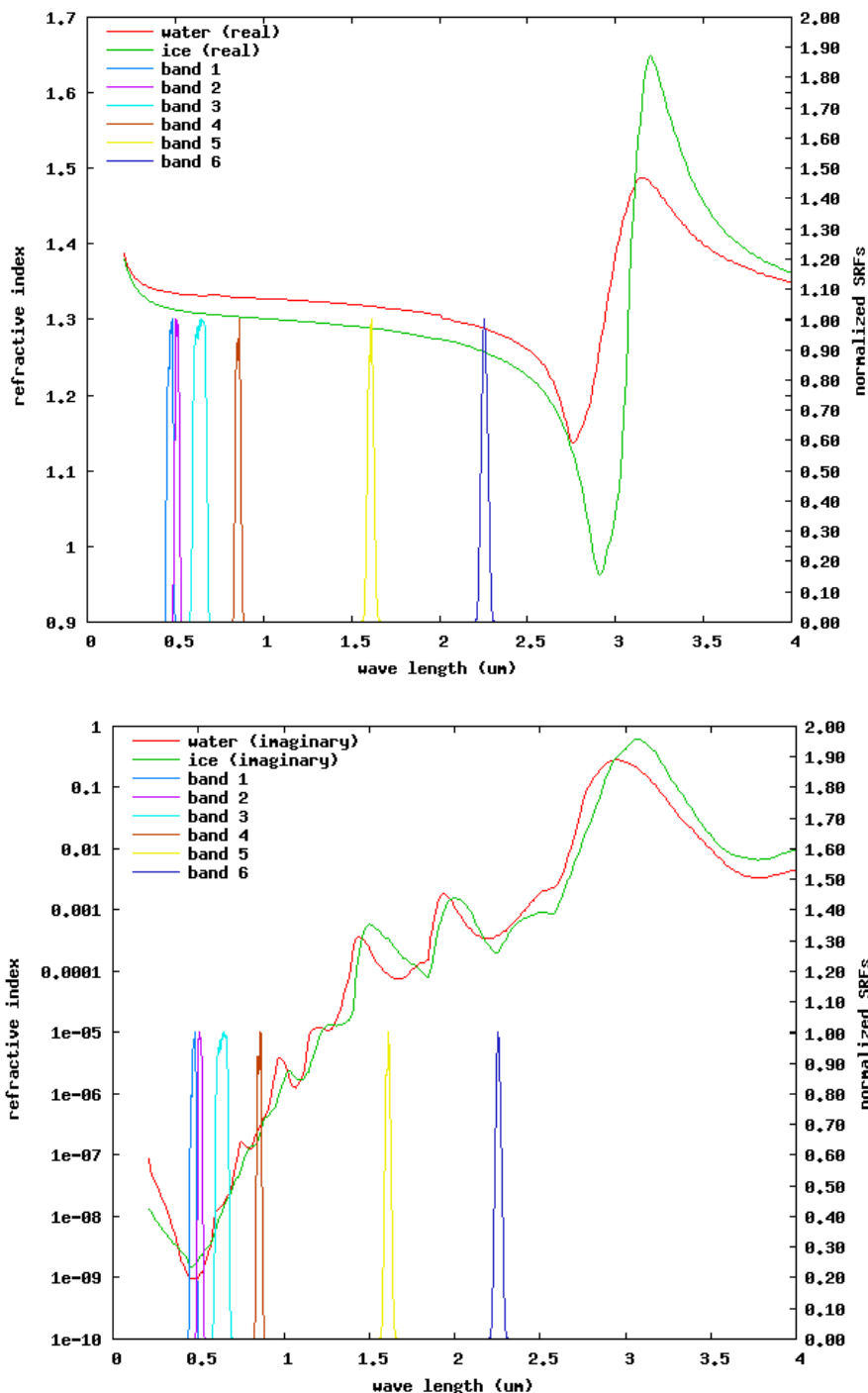


Fig. 1-2-9 Complex refractive index values in visible and near-infrared ranges, and response functions of Himawari-8 AH1 Bands 1 to 6. Top: real part (refractive index); bottom: imaginary part (absorption coefficient).

Reflectance differences related to particle phases in Bands 5 and 6 are accounted for by the complex refractive index (Fig. 1-2-9). The real part of this is simply called refractive index, and the imaginary part is the absorption coefficient, where ice has larger values in Band 5 (yellow) and water is larger in Band 6 (blue).

In Band 5 (Fig. 1-2-10), mid- and lower-level water clouds appear bright, as in Bands 1 to 4.

However, upper-level ice clouds (in red) are relatively dark since their absorption coefficient (green in Fig. 1-2-9) is larger than that of water (in red), which facilitates related identification. Band 6 is also affected by particle phases, while Band 5 generally makes phase determination easier.

Cloud solar reflectance also depends on particle size, especially in Band 6. As per Fig. 1-2-11, greater optical thickness equates to larger solar reflectance in both Bands 3 and 6, and a greater cloud effective radius is associated with a smaller solar reflectance in Band 6 (darker area in red, Fig. 1-2-12). This suggests upper-level ice clouds potentially containing relatively large particles.

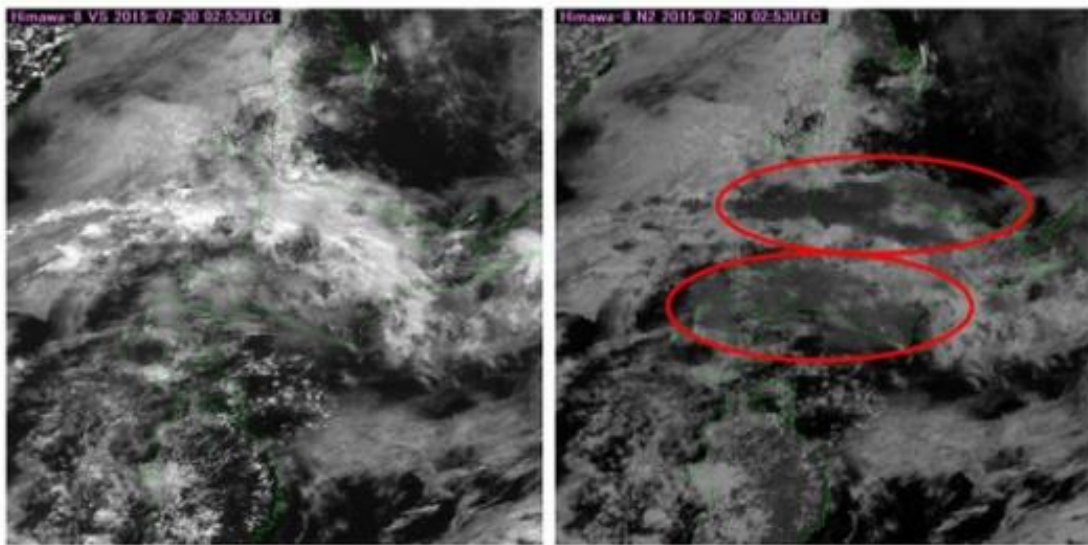


Fig. 1-2-10 Cloud reflection differences associated with cloud particle phases. Left: Band 3; right: Band 5; red: upper-level clouds.

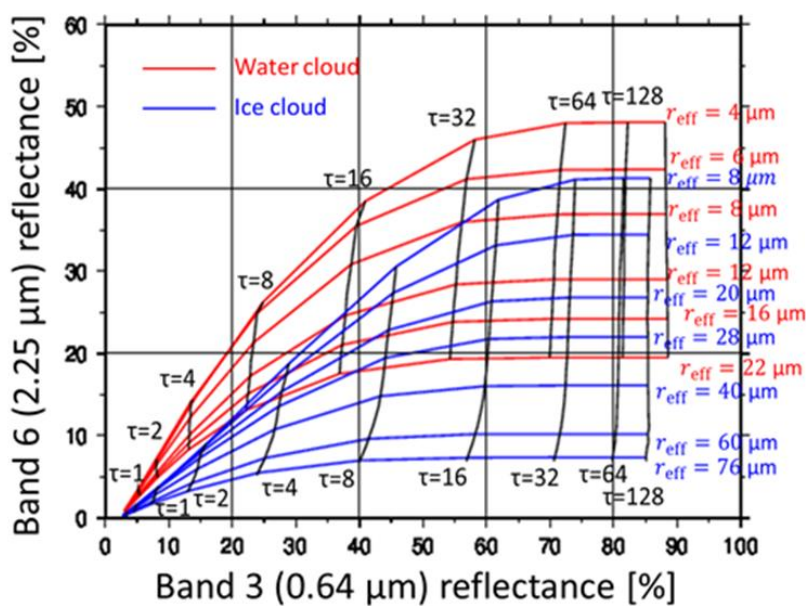


Fig. 1-2-11 Solar reflectance of water/ice clouds in Bands 3 and 6 depending on optical thickness ( $\tau$ ) and effective radius ( $r_{\text{eff}}$ ) via radiative transfer calculation (Hayashi, 2018)

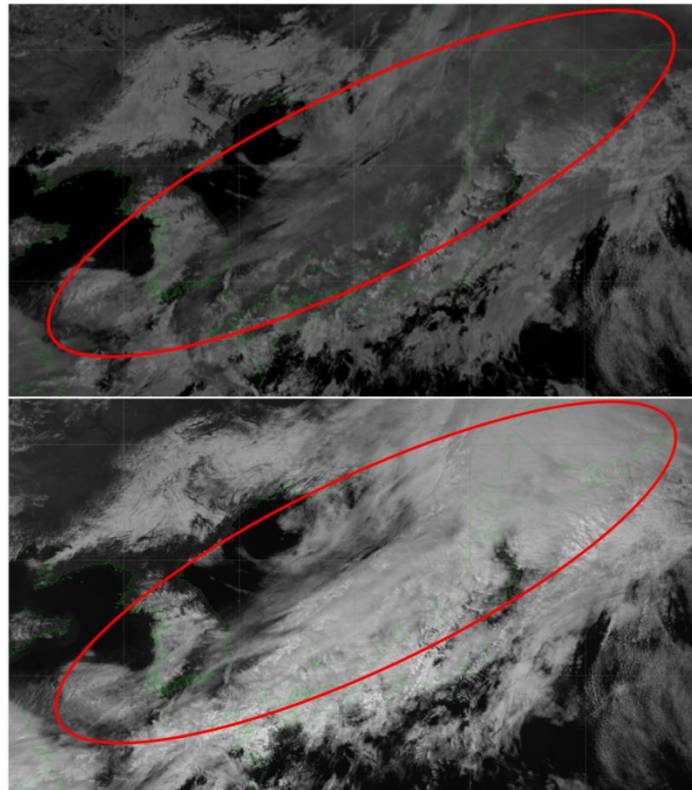


Fig. 1-2-12 Upper-level clouds in Bands 6 (top) and 3 (bottom). Red: upper-level ice clouds.

### C) Hotspot Detection (Bands 5 and 6)

Bands 5 and 6 are responsive to the Earth's radiation only when temperatures are very high, which can be used to detect bright hotspots such as wildfires and volcanoes (Fig. 1-2-13). Hotspots can also be seen using Band 7 (see Section 1.2.3 Infrared Imagery).

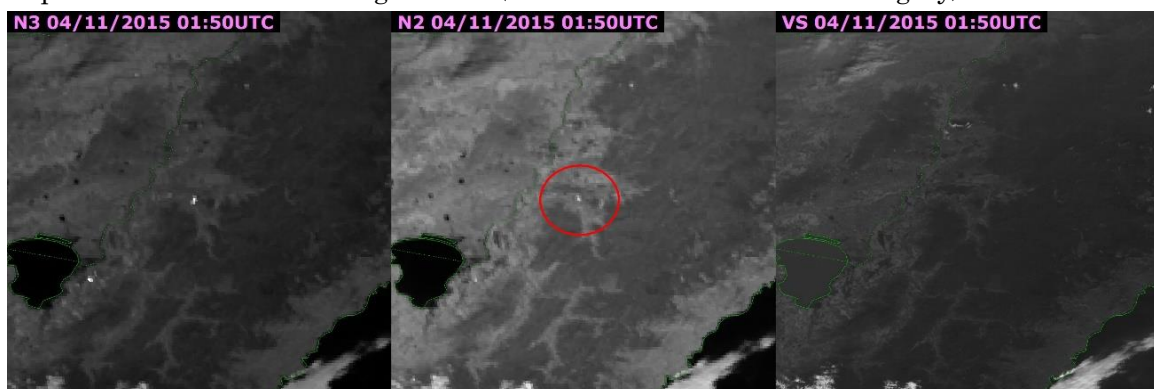


Fig. 1-2-13 Images from Bands 6 (left), 5 (middle) and 3 (right). A wildfire (red; middle) appears in Bands 6 and 5, but not in Band 3.

### (3) Near-Infrared Band Characteristics

- Band 4 (0.86  $\mu\text{m}$ )

## Utilization of Meteorological Satellite Data in Cloud Analysis

- Useful for identifying vegetation, burnt forest areas and other land surface types
- Band 5 (1.6  $\mu\text{m}$ )
  - ⊖ Useful for identifying water phases and differences between lower-level water clouds and upper-level ice clouds or snow/ice-covered land
  - Responsive to hotspots
- Band 6 (2.3  $\mu\text{m}$ )
  - Responsive to cloud particle sizes
  - Responsive to hotspots

## 1.2.3. Infrared Imagery

## (1) Introduction

Observed radiance in Himawari-8/9 AHI infrared bands 7 – 16 consists mostly of Earth’s radiation, and reflected sunlight can largely be ignored (except in Band 7, which consists of both during daytime). Observed radiance in infrared bands is converted to brightness temperature using Planck’s Law with the assumption of blackbody radiation. Infrared imagery is generally rendered so that areas with lower brightness temperatures appear brighter, with clouds appearing bright and sea surfaces appearing dark. Unlike visible and near-infrared bands, infrared bands can be used both day and night, making them suitable for 24-hour observation of clouds and surface temperatures.

As per Fig. 1-2-14, infrared bands are often affected by atmospheric molecule absorption. Bands 8 – 10 are known in particular for relatively strong water vapor absorption, with 10 and 11 being slightly affected by relatively low levels of sulfur dioxide from volcanic and industrial activity. Bands 12 and 16 are affected by ozone and carbon dioxide absorption, respectively, while 7, 11, 13, 14 and 15 (“window bands”) exhibit relatively low absorption. As above, Band 7 is affected by solar reflection in the daytime, and has characteristics differing from those of other infrared bands.

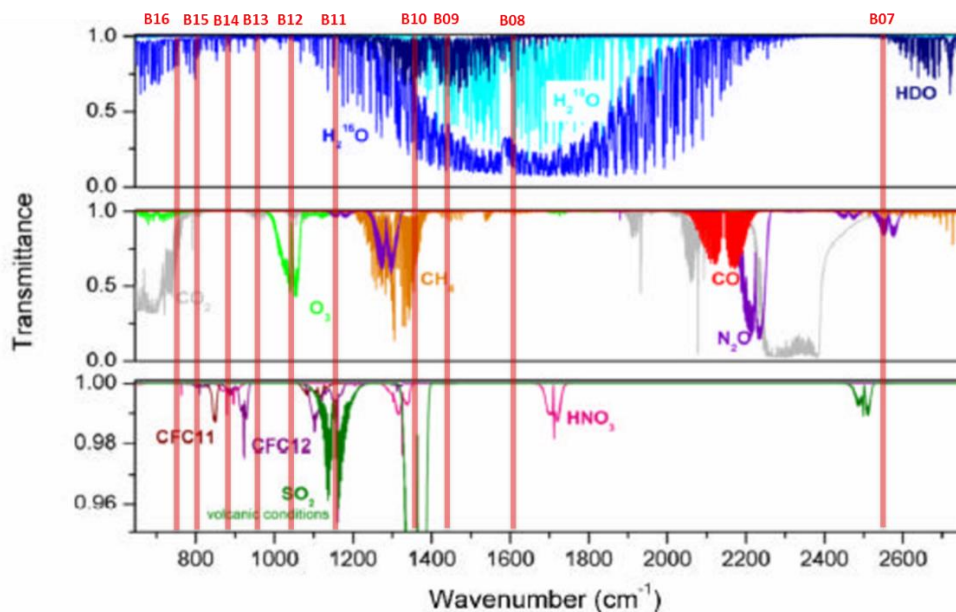


Fig. 1-2-14 Transmittance of major atmospheric molecules in the infrared range. The x-axis represents wavenumbers rather than wavelengths. Red lines indicate the central wavelengths of Himawari-8 AHI Bands 7 – 16 (Clerbaux *et al.*, 2011; amended with additional text).

## (2) Window Bands

The window bands 7, 11, 13, 14 and 15 have weighting functions with peaks at the surface

(Fig. 1-2-15), reflecting their provision of information on the ground surface and in the lower atmosphere.

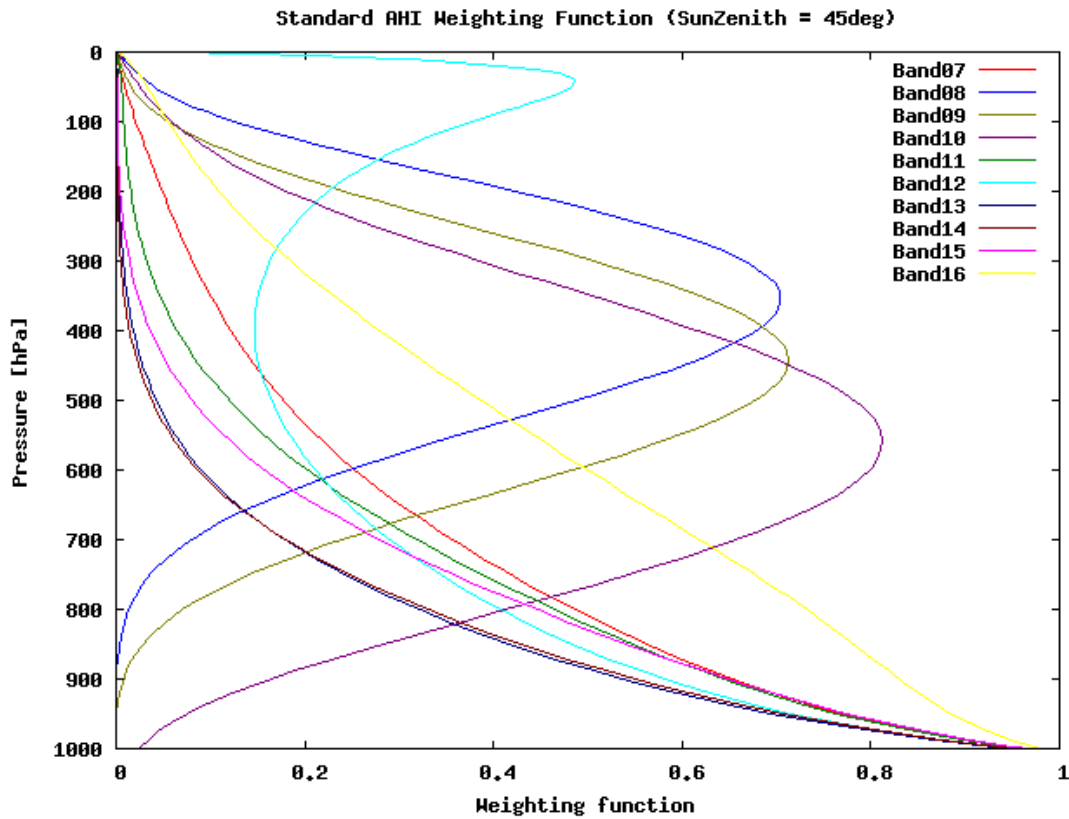


Fig. 1-2-15 Weighting functions of Himawari-8 AHI Bands 7 - 16

Band 7 is called the shortwave window band. Band 7 can be used as one of the window bands only in the nighttime because daytime radiance contains reflected sunlight. The relationship between brightness temperature and radiance here differs from those of other window bands, with Fig. 1-2-16 showing this (left) against Band 13 (right). The latter shows practical linearity for 220 to 300 K, while Band 7 exhibits nonlinearity. Accordingly, small changes in low radiance values can cause large changes in brightness temperature in Band 7, resulting in reduced resolution below 230 K in particular. As a result, cumulonimbus and thick upper clouds may exhibit dot noise in Band 7 and related difference imagery (Fig. 1-2-17).

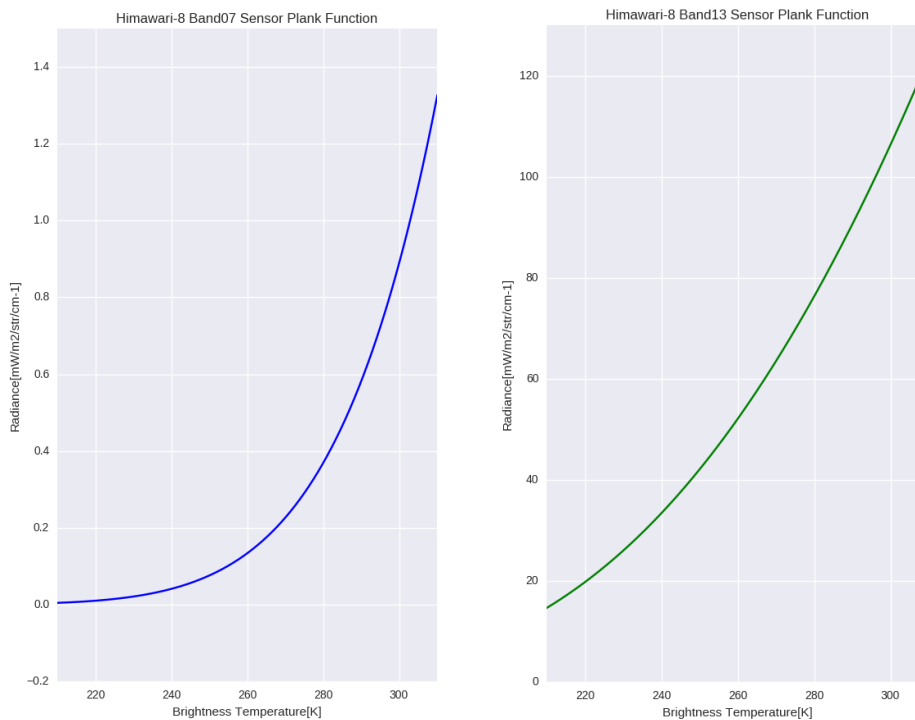


Fig. 1-2-16 Brightness temperature vs. radiance in Bands 7 (left) and 13 (right)

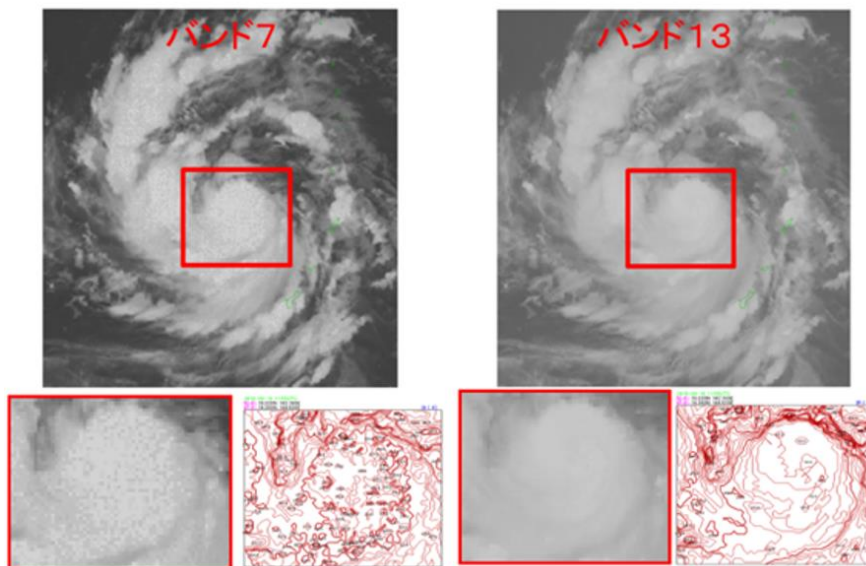


Fig. 1-2-17 Noise in Band 7 (left) in a low brightness temperature area around the center of Typhoon Goni in 2015, and Band 13 image (right)

Bands 11, 13, 14 and 15 are called the longwave window bands, with Band 11 being more affected by water vapor absorption and sulfur dioxide. This band is useful for distinguishing cloud particle phases (as described later), and bands on other sensors with similar central

wavelengths are sometimes called “cloud-top phase bands”. Figure 1-2-14 indicates that the central wavelength of Band 13 has a transmittance closer to 1 than Bands 14 and 15, making it suitable for subjective cloud analysis. Thus, Band 13 is sometimes called a “clean” window band. Imagery showing differences between Band 13 and others can also be revealing, while Band 15 is more known as a “dirty” window band for its lower transmittance than 13 and 14, which have similar central wavelengths to 13 (Fig. 1-2-18) and provide comparable imagery. However, differences in absorption coefficients (Fig. 1-2-19), surface emissivity (Fig. 1-2-20) and atmospheric transmittance (Fig. 1-2-14) are seen, as per the upper clouds with lower brightness temperatures in Fig. 1-2-21.

Bands 13 and 15 will replace IR1 and IR2 on MTSAT-2, respectively, due to their higher correlations than adjacent bands, while IR4 on MTSAT-2 will be replaced by Band 7 (Murata et al., 2015).

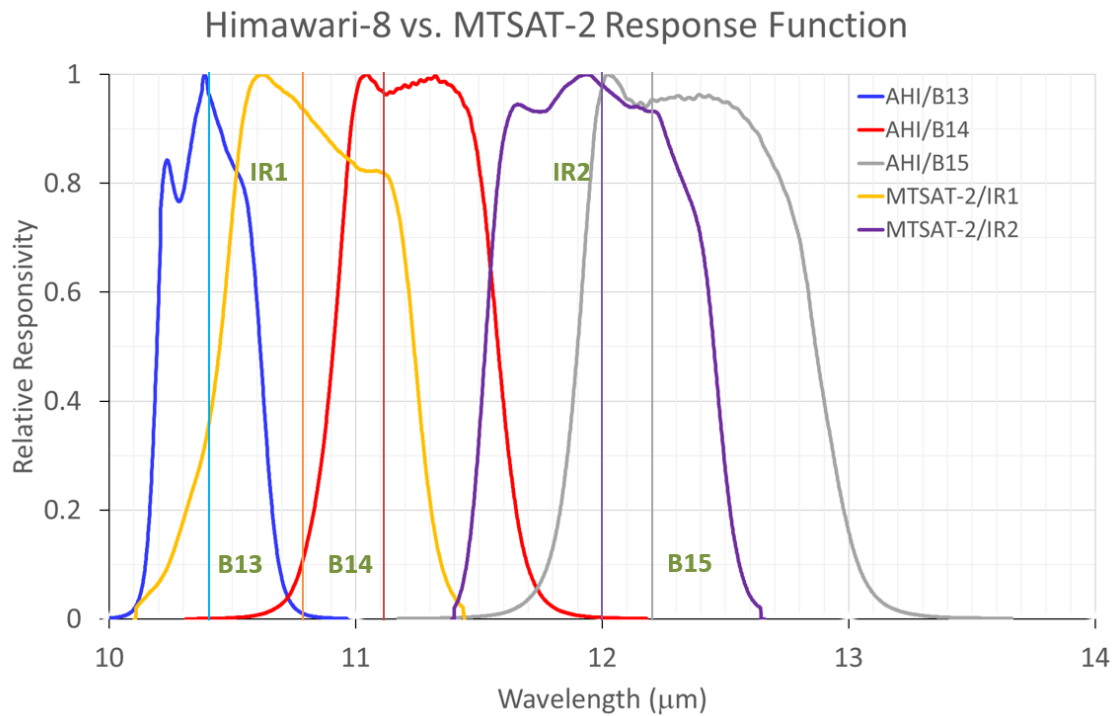


Fig. 1-2-18 Response functions of bands 13 (blue) 14 (red) and 15 (gray) on Himawari-8 and IR1 (yellow) and IR2 (purple) on MTSAT-2. Vertical lines are centre wavelengths.

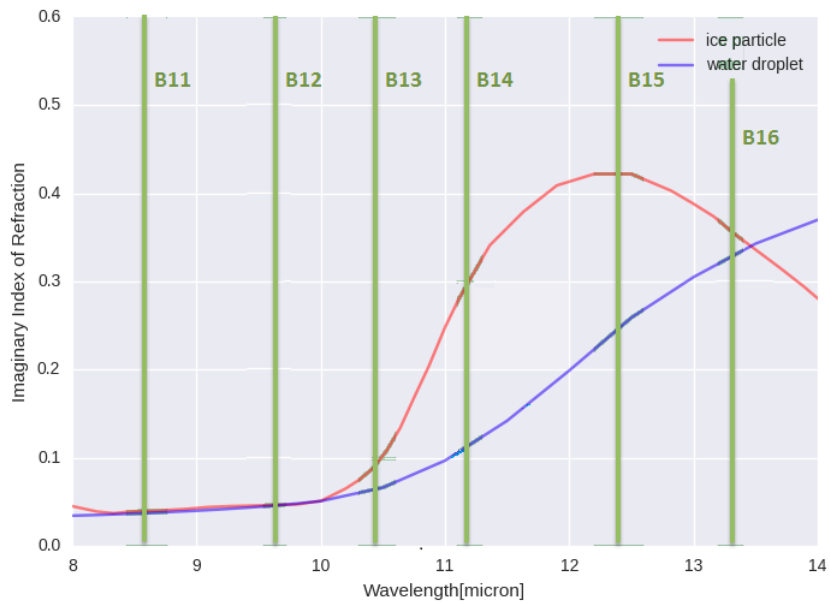


Fig. 1-2-19 Imaginary part of complex refractive index (i.e., absorption coefficients) for water and ice between 8 and 14  $\mu\text{m}$  (Hale and Querry, 1973 for water; Warren, 1984 for ice).

Vertical lines: central wavelengths of Himawari-8 AHI bands 11 to 16.

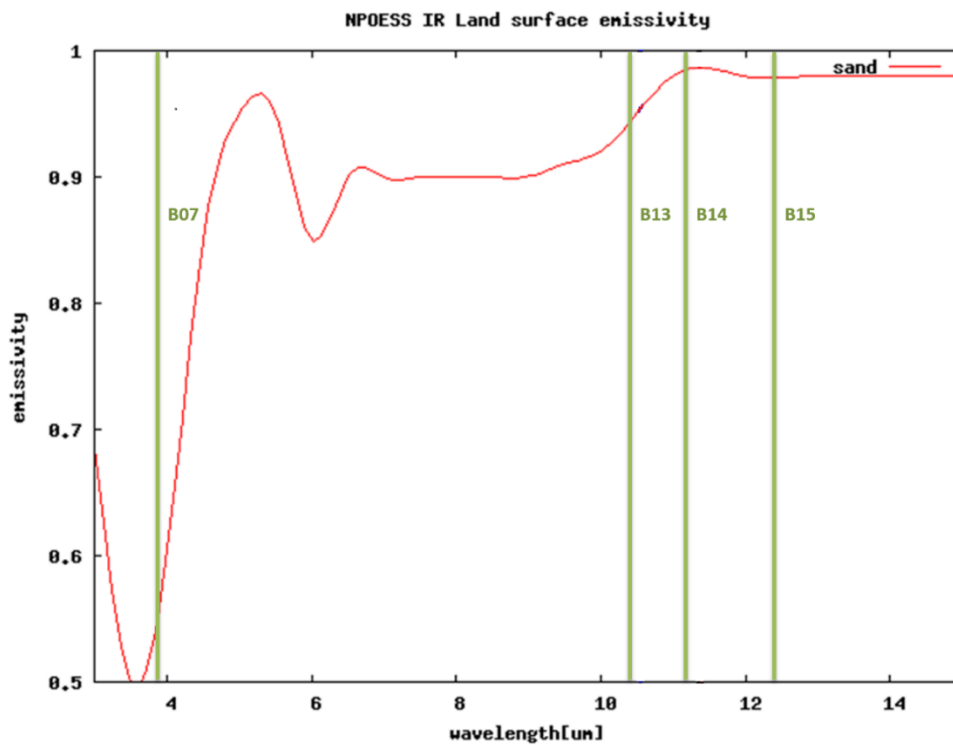


Fig. 1-2-20 Sand emissivity between 3 and 15  $\mu\text{m}$  in CRTM. Vertical lines: central wavelengths of Himawari-8 AHI bands 7, 13, 14 and 15.

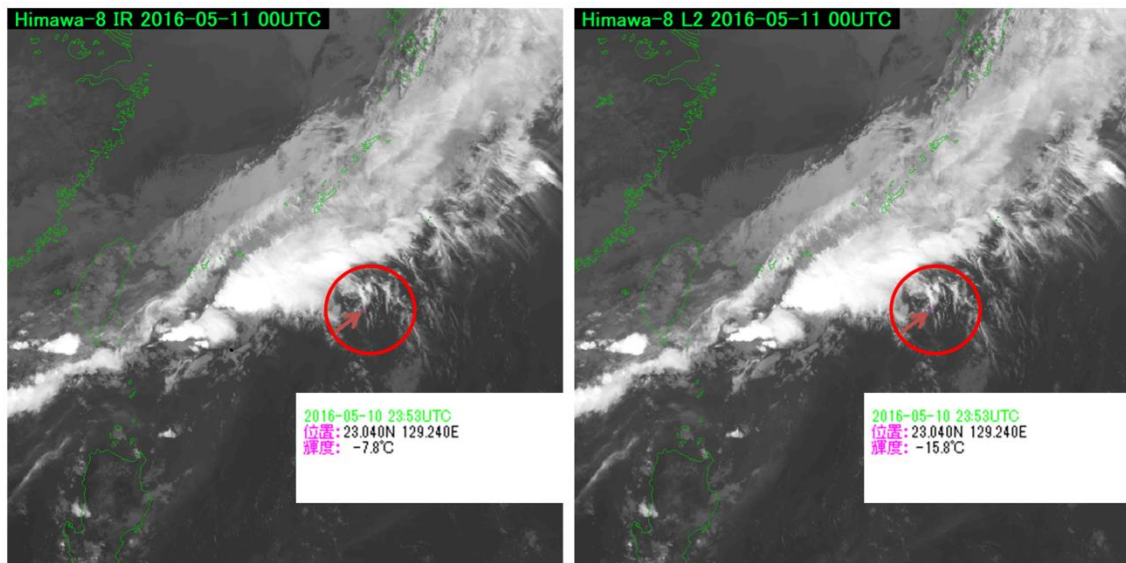


Fig. 1-2-21 Band 13 (left) and 14 (right) images indicating brightness temperatures of  $-7.8$  and  $-15.8^{\circ}\text{C}$ , respectively.

### (3) Water Vapor Bands

Bands 8, 9, and 10 are called water vapor bands. Water vapor imagery corresponds to the amount of water vapor between the upper and middle troposphere because it is affected by a relatively strong absorption of water vapor. The weighting functions in Fig. 1-2-15 show that each water vapor band has a different peak altitude, suggesting that the observed water vapor altitudes are different. However, it should be noted that these bands do not represent only water vapor at a peak altitude of a weighting function, but rather a distribution with some depth (Kumabe, 2006).

As can be seen from the weighting functions (Fig. 1-2-15), Band 8 has a peak around 300 to 400 hPa in the standard atmosphere. This altitude corresponds to the upper troposphere, and it is the highest among the water vapor bands. Band 9 has a peak around 400 to 500 hPa, which corresponds to the upper and middle troposphere. Band 10 has a peak around 500 to 600 hPa, which corresponds to the middle troposphere, and it is the lowest among the water vapor bands. Also, according to Fig. 1-2-14, Band 8 has the smallest water vapor transmittance, followed by Bands 9 and 10. Comparing the overall brightness of Bands 8, 9, and 10 in Fig. 1-2-22, Band 8 is the brightest (i.e., the highest brightness temperature) as it is the most affected by the water vapor in the upper layer.

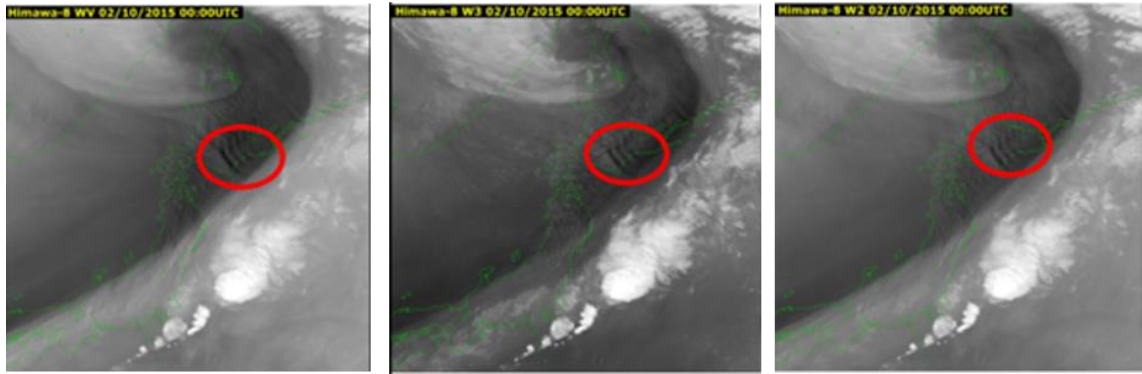


Fig. 1-2-22 Wave patterns corresponding to mountain lee waves in water vapor imagery (red oval). Bands 8, 9 and 10 from left to right.

By using Bands 8, 9, and 10 together, it is possible to understand the three-dimensional distribution of water vapor to some extent.

Taking Band 8 which mainly corresponds to water vapor in the upper troposphere as an example, the standard atmosphere is simplified into three layers: upper, middle, and lower, and the amount of infrared absorption and emission is schematically shown (Fig. 1-2-23). From near the ground surface to the lower layers of the atmosphere, the air is hot and contains a lot of water vapor, so a large amount of infrared radiation is emitted. However, at the same time, most of it is absorbed by water vapor, and only a small amount of infrared radiation reaches the satellite. As altitude increases, both the temperature and the amount of water vapor decrease, so less infrared radiation is emitted, but absorption by water vapor is also reduced. In the upper layers, both the temperature and the amount of water vapor are even lower, so the amount of emitted infrared radiation is small, but it reaches the satellite almost without being absorbed.

Dry areas with little water vapor in the upper and middle layers show high brightness temperatures and appear dark because a large amount of radiation from the lower layers reaches a satellite almost unabsorbed. Humid areas with a lot of water vapor in the upper and lower layers show low brightness temperatures and appear bright because radiation from clouds and water vapor in the upper and middle layers is dominant. Figure 1-2-24 shows the characteristics of water vapor imagery related to atmospheric phenomena.

From the perspective of radiative characteristics, JMA has chosen Band 8 as a successor to IR3 on MTSAT-2 (Murata et al., 2015).

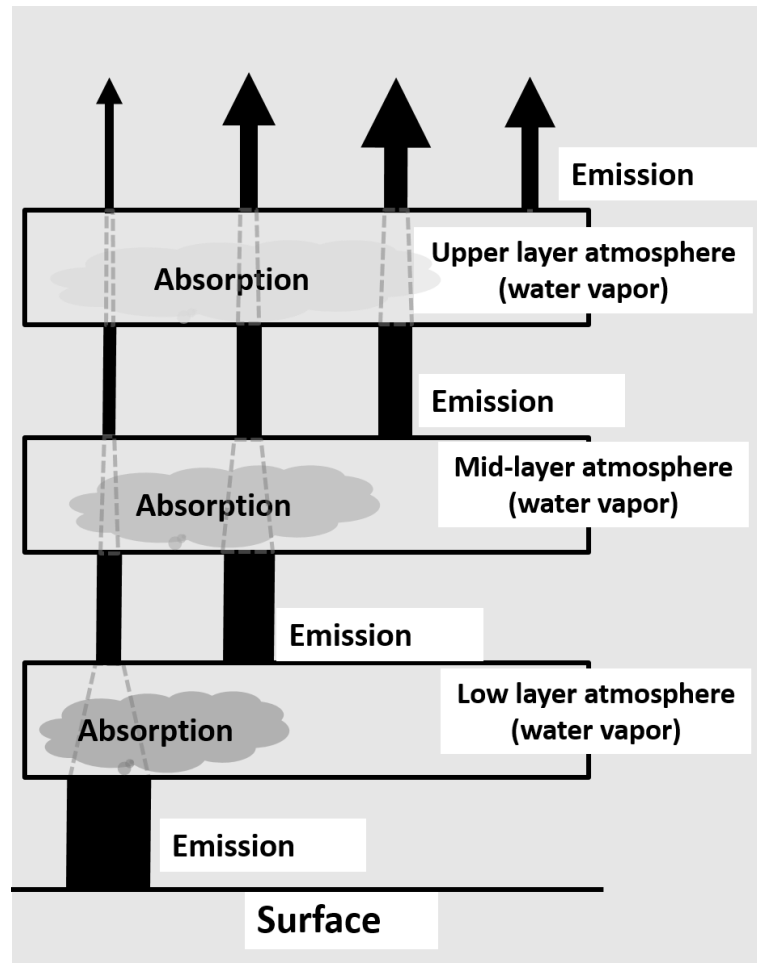


Fig. 1-2-23 Conceptual diagram of radiation in water vapor imagery (Kishimoto, 1997)

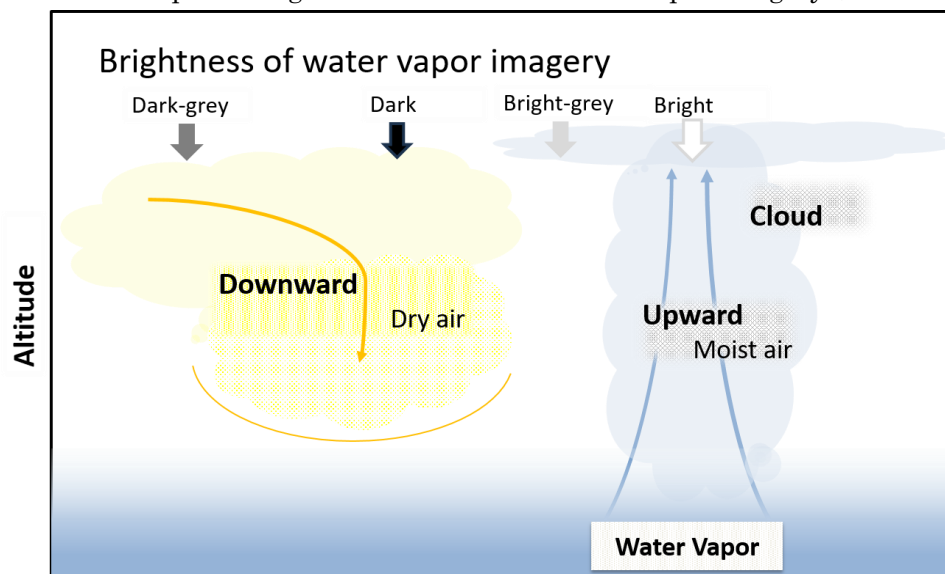


Fig. 1-2-24 Schematic relationship between atmospheric phenomena and appearance in water vapor imagery

(4) Infrared Imagery Usage

### A) 24-hour Observation (All Bands)

As mentioned above, infrared bands are available both day and night. Moreover, we can consider that observed radiance in Bands 8-16 contains only Earth's emission and is not affected by solar reflection. This makes it easier to use these bands for 24-hour observation.

### B) Cloud Top Height Estimation (Window Bands)

Normally, satellite observations of clouds reveal only their tops, and brightness temperatures of clouds in infrared window band imagery can be considered as temperatures of their tops. Cloud top temperatures can be converted to cloud top heights by combining them with vertical temperature profiles obtained from objective analysis and numerical weather prediction. In the troposphere, except for inversion layers, temperatures are generally lower in the upper layer, suggesting that clouds with lower cloud top temperatures have higher cloud top heights. Vertical development of clouds can be detected by monitoring changes in cloud top temperature. Note that it may be difficult to apply this estimation to some clouds, such as vertically developed cumulonimbus clouds seen from an angle and thin cirrus clouds.

### C) Land/Sea Surface Temperature Estimation (Window Bands)

Land and sea surface temperature can also be estimated from infrared window band imagery only when not covered by clouds. Sea surface temperature in the open ocean derived by satellite observation is particularly valuable information because there are few in-situ observations.

### D) Reflected Sunlight Component (Band 7, Only in the Daytime)

The wavelength around 3.9  $\mu\text{m}$  is largely affected by sunlight reflection. For this reason, an observed radiance of Band 7 contains both reflected sunlight and Earth's radiation in the daytime.

Generally, according to Fig. 1-2-25, 3.9  $\mu\text{m}$  reflectance of clouds is larger when the particle size is smaller, and water clouds show larger reflectance than ice clouds. Among the water clouds, those over the sea surface usually have larger particle sizes and show smaller reflectance than those over the land. This feature can be used to distinguish the cloud particle size and phase. However, contamination of Earth's radiation makes it harder to distinguish them by only Band 7 imagery. To solve this problem, the method for extracting the reflected sunlight component of 3.9  $\mu\text{m}$  by using the other window band around 10  $\mu\text{m}$  has been devised (Rosenfeld, 2004). JMA applies this method for Band 7 using Band 13 as a 10  $\mu\text{m}$  band. As shown in the Band 7 image in Fig. 1-2-26, the upper clouds (red arrow) consisting of ice appear brighter mainly because of their lower temperatures and smaller reflectance, and the lower clouds (blue arrow) appear darker. The reflected sunlight component image reveals that the

upper clouds reflect less sunlight, and the lower clouds reflect more. The reflected sunlight component of Band 7 is also utilized in RGB imagery.

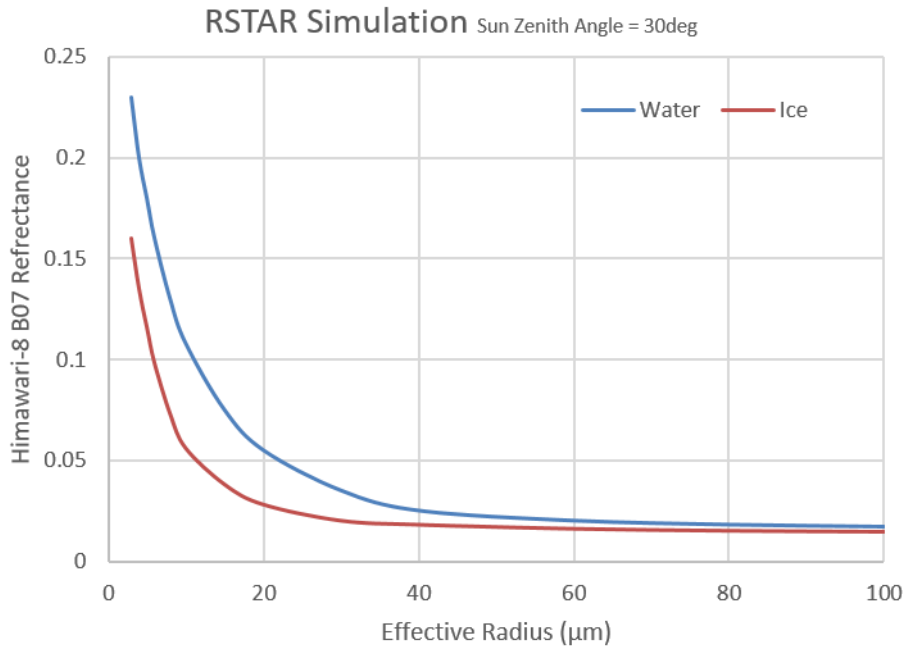


Fig. 1-2-25 3.9 µm reflectance of clouds depending on phase (water and ice) and effective radius simulated by the radiative transfer model RSTAR (Nakajima and Tanaka, 1986, 1988; Stamnes *et al.*, 1988)

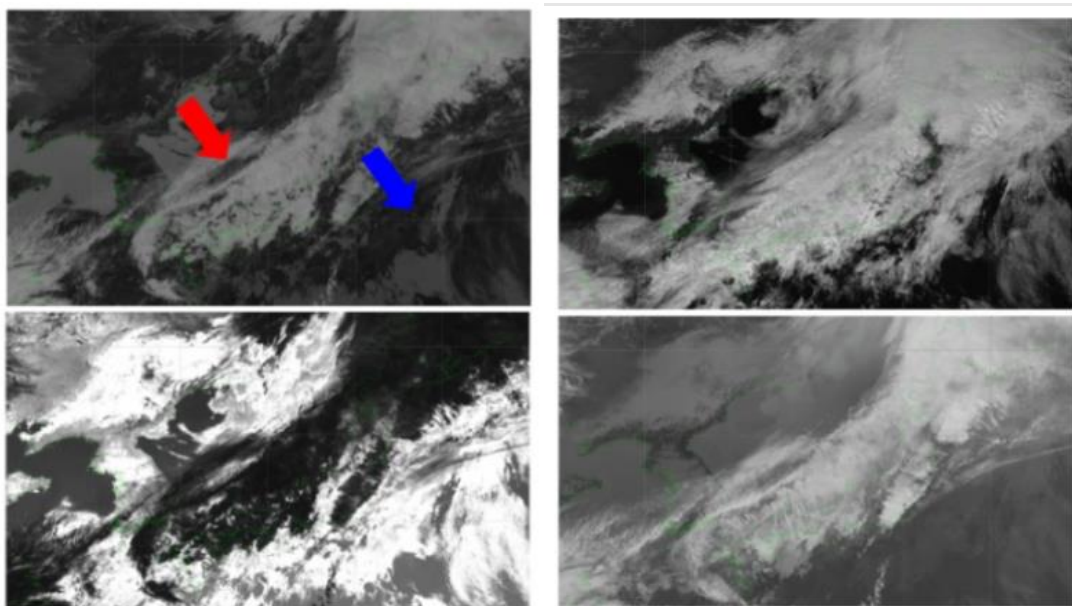


Fig. 1-2-26 Example of Band 7 (upper left) image and an image acquired by the method from Rosenfeld (2004) (lower left). Images of Band 3 (top right) and Band 13 (bottom right) at the

same time. Note that the lower left image has been rendered so that areas with larger reflectance are brighter, which is the same way as visible and near-infrared imagery.

E) Hotspot Detection (Band 7)

High-temperature heat sources such as wildfires, volcanoes, and industrial areas may appear as tiny dark areas in Band 7 (and tiny bright areas in Bands 5 and 6).

As shown in Fig. 1-2-27, radiance in Band 7 exponentially rises as blackbody temperature increases, while radiance in Band 13 gradually rises. In other words, if the target is hot enough, observed radiance in Band 7 will be highly sensitive to its temperature change. Assuming an area corresponding to one pixel of satellite observation, if a temperature of half of it is 300 K and the other half is 500 K, the brightness temperature of the entire pixel is not the arithmetic mean of them (400 K) but is approx. 420 K in Band 13 and approx. 460 K in Band 7 (Fig. 1-2-28). According to the above, hotspots appear even if heat sources are smaller than a pixel. In the example (Fig. 1-2-29), hotspots can be seen as tiny dark areas.

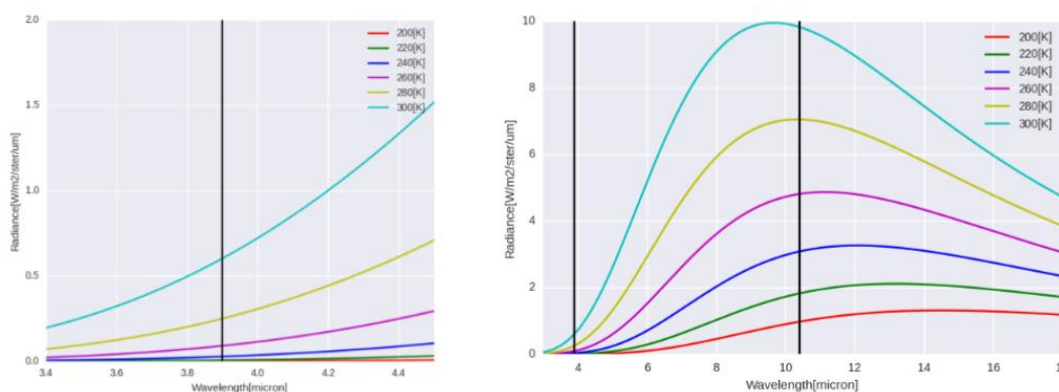


Fig. 1-2-27 Radiance of blackbodies at various temperatures in the spectral range from 3.4 to 4.5  $\mu\text{m}$  (right panel) and from 3 to 18  $\mu\text{m}$  (left panel), obtained from Planck's law. Black lines indicate central wavelengths of Himawari-8 AH Band 7 in right panel, Band 13 in left panel, respectively.

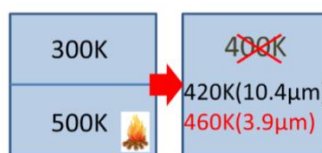


Fig. 1-2-28 Schematic diagram of satellite observation in Bands 7 (3.9  $\mu\text{m}$ ) and 13 (10.4  $\mu\text{m}$ ) of a pixel that half of it is 300 K and the other half is 500 K

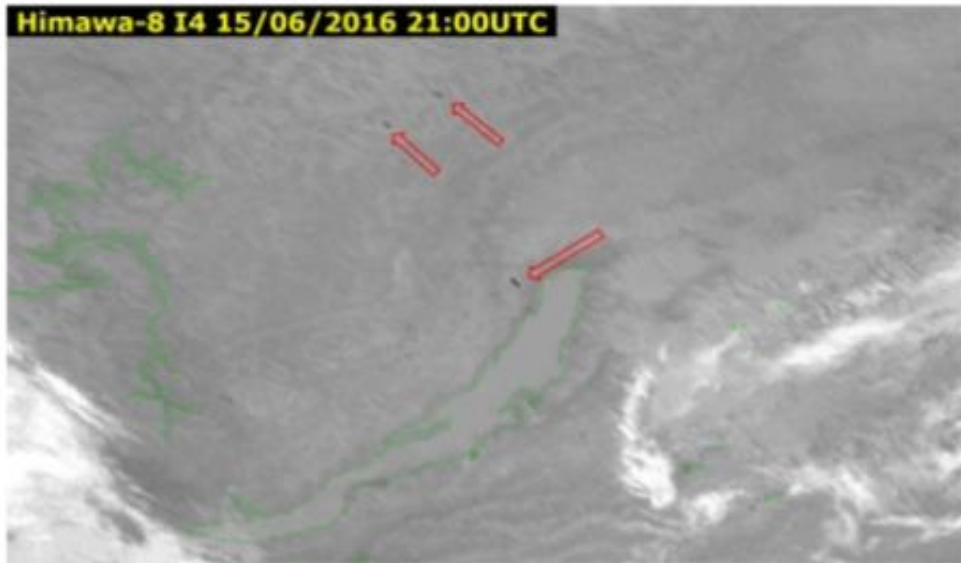


Fig. 1-2-29 Example of hotspots (wildfire near Lake Baikal) in Band 7

F) Fog Detection (Difference between Bands 7 and 13, Only in the Nighttime)

According to Fig. 1-2-30, the emissivity of stratocumulus/fog is smaller in 3.8  $\mu\text{m}$  (equivalent to Band 7) than in 11  $\mu\text{m}$  (equivalent to Bands 13 or 14), resulting in the observed brightness temperature being lower in Band 7 in the nighttime than in Band 13. Generally, difference imagery between Bands 7 and 13 is made by subtracting the brightness temperatures of Band 13 from Band 7, and areas with negative values are rendered as bright areas. Therefore, difference imagery between Bands 7 and 13 reveals potential stratocumulus/fog areas as bright areas, and it can be used for fog monitoring.

Figure 1-2-31 shows a case of fog or the lower clouds spread over the Seto Inland Sea. Though fog was observed in the surface observation around the Seto Inland Sea, it is difficult to identify fog areas by a Band 13 image. On the other hand, a difference image between Bands 7 and 13 shows bright areas with distinct edges corresponding to areas with fog/mist observation.

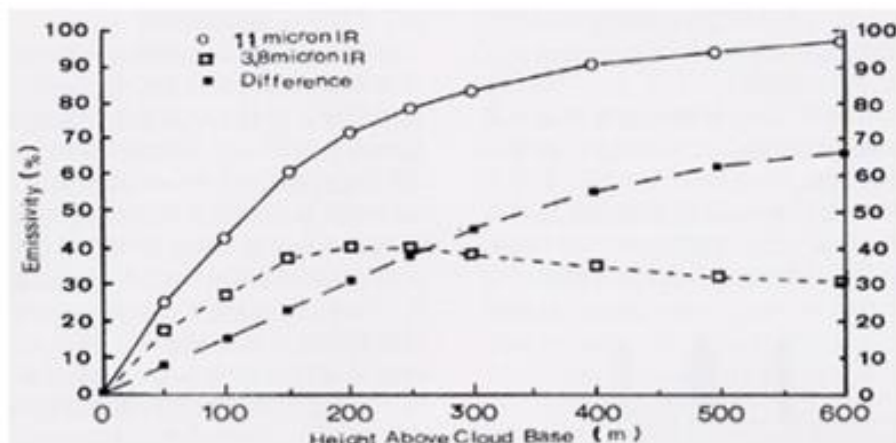


Fig. 1-2-30 Relationship between height above cloud base (i.e., cloud thickness) of stratocumulus of cloud water content  $0.1 \text{ gm}^{-3}$  and the emissivity (Ellrod, 1995)

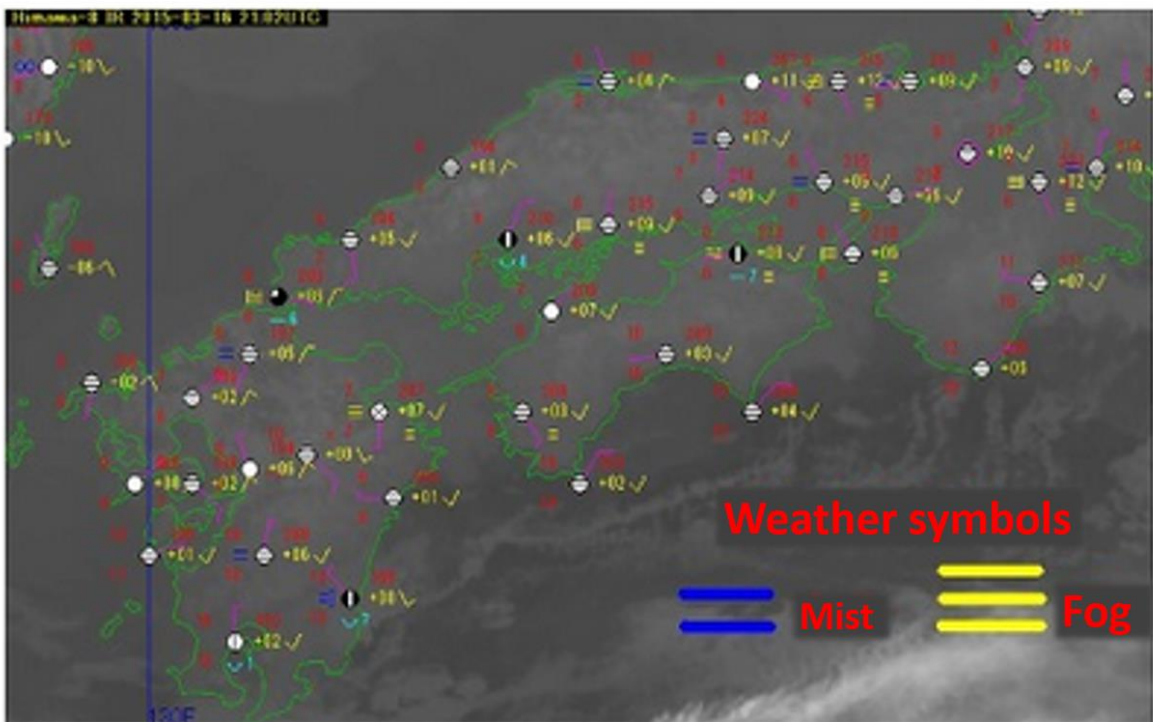
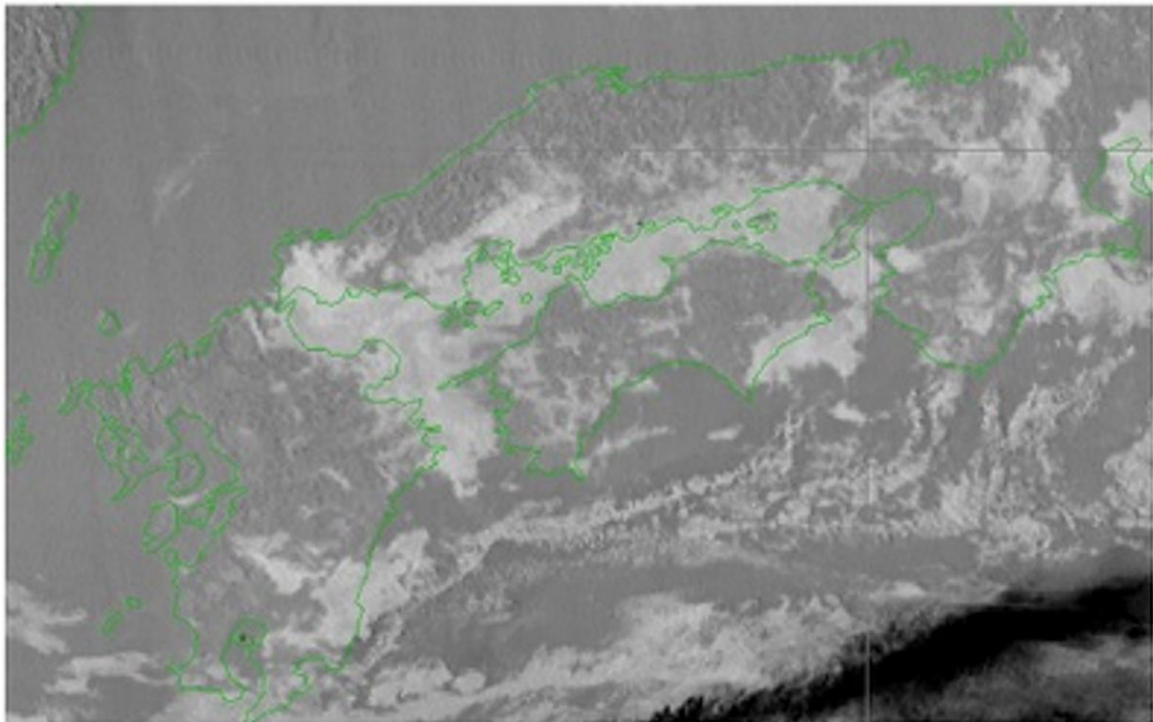


Fig. 1-2-31 Fog around the Seto Inland Sea. Top: a difference image between Bands 7 and 13; bottom: Band 13 with surface observation data.

G) Upper-cloud Distinction between Bands 7 and 13; Nighttime

At night, radiation from the relatively high-temperature earth surface penetrates thin higher clouds, adding to radiation from the cloud top. Accordingly, the cloud top temperature in Band 7 is higher than the actual value. As the transmission effect is larger for Band 7 than for Band 13, the cloud top temperature is higher than the infrared temperature, and the related difference is positive. In difference imagery, upper clouds appear differently mainly depending on their thickness. Thin upper clouds transmit radiation from below and appear to have a brightness temperature higher than the actual cloud top temperature (Fig. 1-2-32, MSC, 2005). It is possible to distinguish between cumulonimbus, which brings rainfall, and anvil cirrus, which does not.

Thick upper clouds do not transmit significant radiation from below, and brightness temperature is as low as cloud top temperature, resulting in dot noise as described previously.

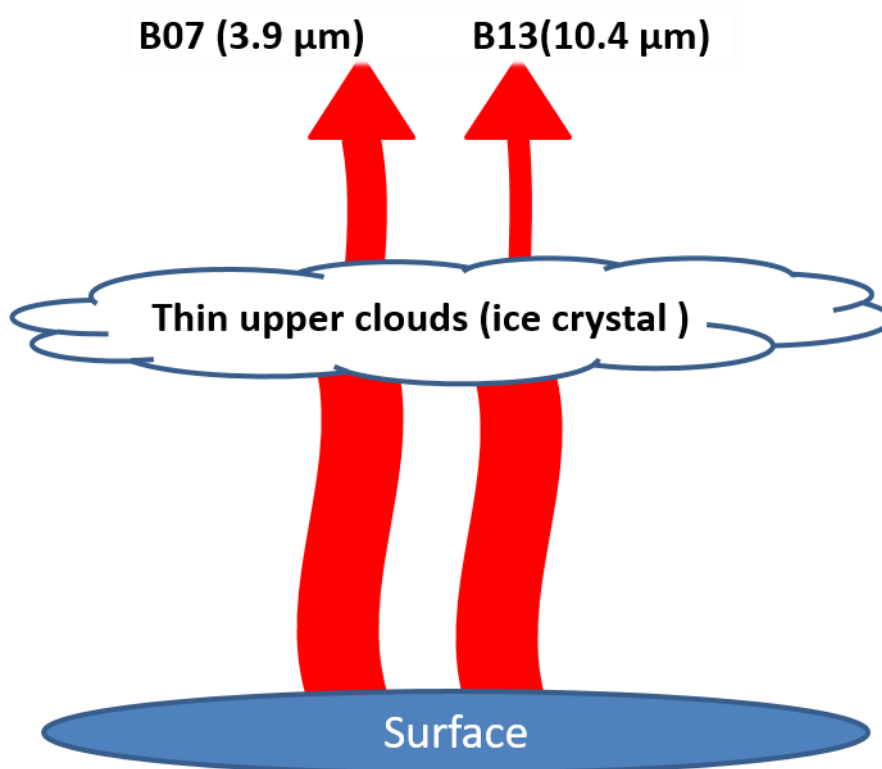


Fig. 1-2-32 Radiation through thin upper clouds in Bands 7 and 13 (MSC, 2005)

H) Land Surface Distinction between Bands 7 and 13; Nighttime

In this difference imagery, land surfaces may display certain characteristics because of emissivity differences between Bands 7 and 13. For example, the emissivity of sand is lower in Band 7 (Fig. 1-2-20), resulting in desert areas appearing bright as per Fig. 1-2-33.

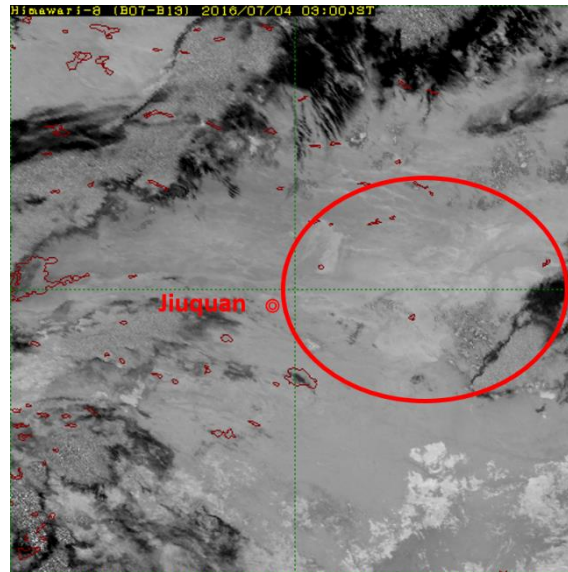


Fig. 1-2-33 Difference image between Bands 7 and 13 around the Gobi Desert at night. The desert area (red circle) appears brighter.

I) Atmospheric Characteristics in Upper/Middle Layers (Water Vapor Bands)

Atmospheric currents can be visualized in water vapor imagery using water vapor as a tracer, with bright and dark areas indicating upper to middle-level troughs, ridges, vortices and jet streams. Temporal changes in these areas enable estimation of trough deepening in upper to middle layers and the strength of subsidence in dry regions.

J) Observation of Wave Patterns (Water Vapor Bands)

The spatial resolution of infrared imagery at the sub-satellite point from Himawari-8/9 has been enhanced from the previous 4 km to 2 km, making phenomena easier to identify. As per Fig. 1-2-22, wave patterns (in red) are often found in water vapor imagery in correspondence with mountain lee waves, which provide important information for aircraft operations (MSC, 2002).

K) Sulfur Dioxide Monitoring (Bands 10 and 11)

As per Fig. 1-2-14, Bands 10 and 11 are sensitive to absorption by sulfur dioxide molecules. Figure 1-2-34 shows a volcanic eruption, with plume appearance being clearer in Bands 10 and 11 than in Band 8. The appearance is also distinctive in Bands 13 and 15, indicating potential other plume content such as water vapor and volcanic ash (due to the continuous water vapor absorption zone around the central wavelength of Band 13). Bands 11 and 13 show that the eastern part of the plume appears darker than the western part, suggesting more sulfur dioxide in the former.

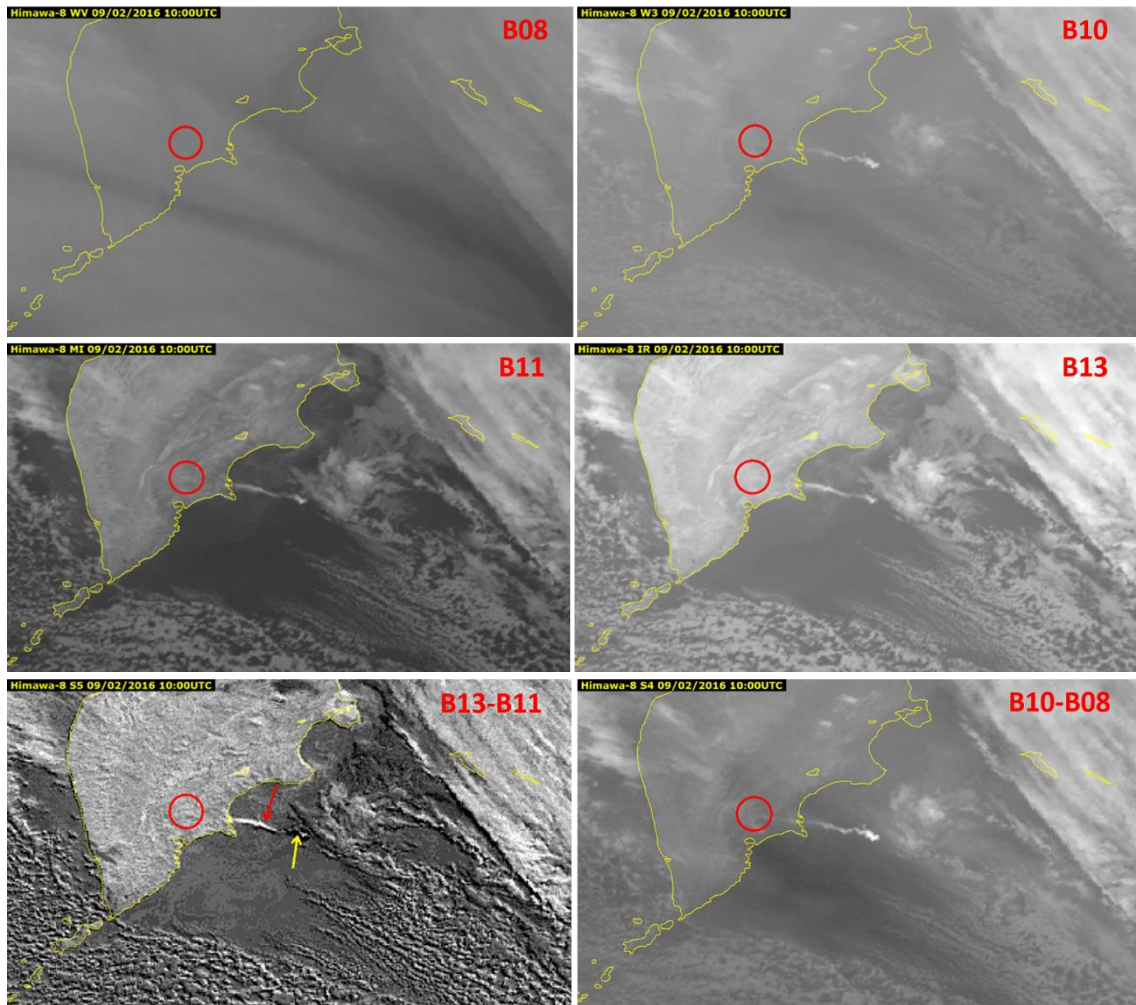


Fig. 1-2-34 Zhupanovsky eruption (red) on the Kamchatka Peninsula

L) Cloud Phase Distinction (Bands 11 and 15)

Band 11 imagery is more useful for estimating cloud particle phases than other window bands (e.g., Bands 13 and 14). As per Fig. 1-2-35, brightness temperature difference using Band 11 shows a much more noticeable difference between cloud particle phases than that of Band 15. Band 11 shows higher emissivity than Band 14 (Fig. 1-2-36) for upper ice clouds, resulting in a higher brightness temperature. Lower water clouds and sea surfaces exhibit lower brightness temperatures in Band 11 due to lower water vapor absorption and differences in emissivity, which supports cloud phase distinguishment. Accordingly, JMA/MSM uses Band 11 to obtain cloud particle phase information for cloud products.

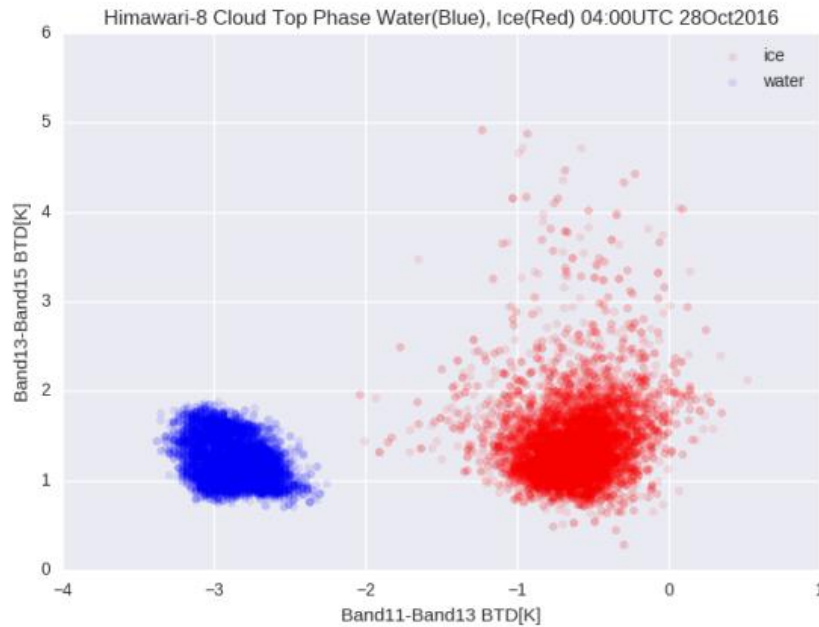


Fig. 1-2-35 Brightness temperature differences for tops of clouds consisting of ice (red) and water (blue). X-axis: Bands 11 – 13; Y-axis: Bands 13 – 15.

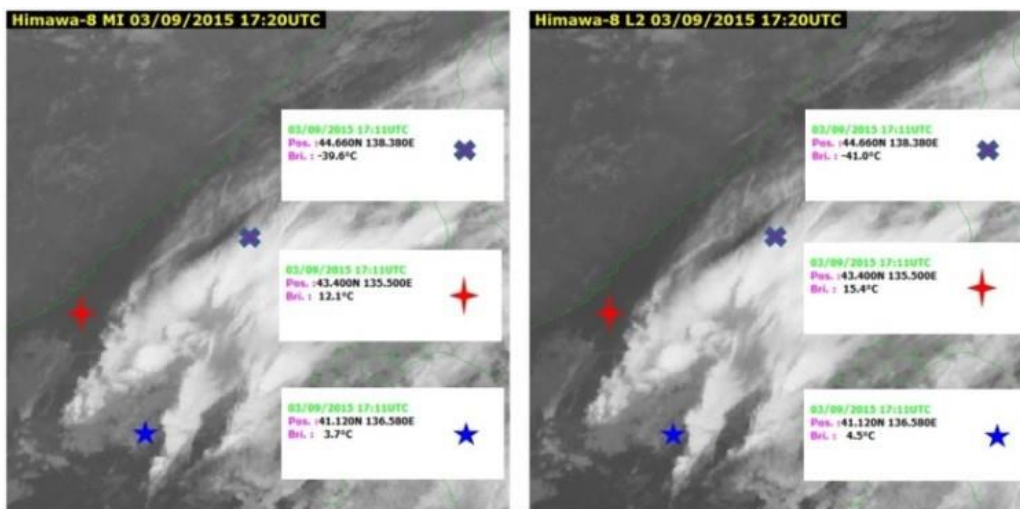


Fig. 1-2-36 Brightness temperature comparison between Bands 11 (left) and 14 (right) Red crosses: thick high ice clouds; blue stars: low-level clouds; plus marks: clear conditions.

In Band 15, differences in absorption coefficients between water and ice crystals due to cloud phase are larger than in other window bands (Fig. 1-2-19). This makes the brightness temperature lower in thin upper clouds. Difference imagery in areas with large Band 13 – 15 values are therefore dark, making thin upper clouds appear darker (Fig. 1-2-37).

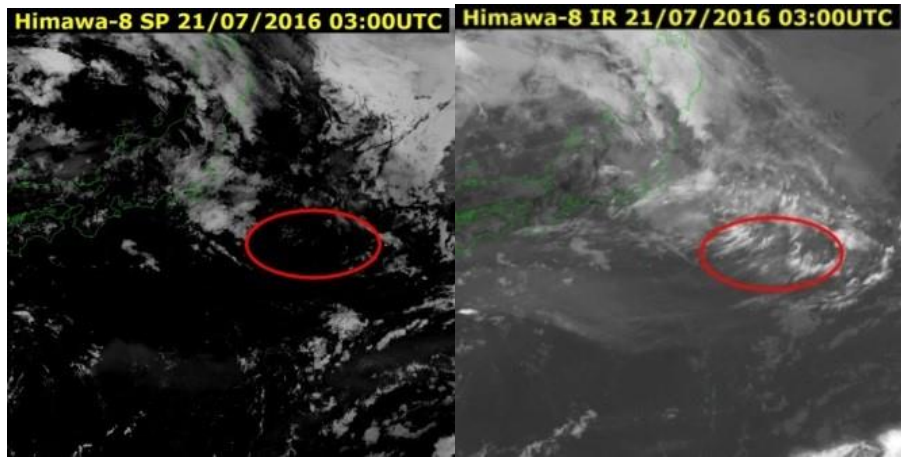


Fig. 1-2-37 Upper clouds in difference imagery between Bands 13 and 15 (left), and a Band 13 image (right). Red: thin upper clouds.

#### M) Ozone Analysis (Band 12)

As per Fig. 1-2-14, Band 12 is sensitive to absorption by ozone molecules, making its weighting function have a stratospheric peak above 100 hPa. Generally, ozone molecules are generated in the stratosphere in the tropics and transported to middle and high-latitude regions by Brewer-Dobson circulation, which have relatively large amounts of ozone except for the Antarctic region where the ozone hole is located. As per Fig. 1-2-38, Band 12 has a larger color gradient from low to high-latitude regions than Band 13, partially due to this ozone distribution. In Band 12 imagery, white stripes may appear in areas corresponding to dark areas of water vapor imagery, as per Fig. 1-2-39 (upper right, circled in yellow). The positive 300 hPa vorticity in the figure supports a conclusion of high ozone concentration at relatively low heights and potential tropopause folding (Zwatz-Maise, 2004). Difference imagery between bands 12 and 13 shows darker shades (lower left, Fig. 1-2-39, circled in yellow).

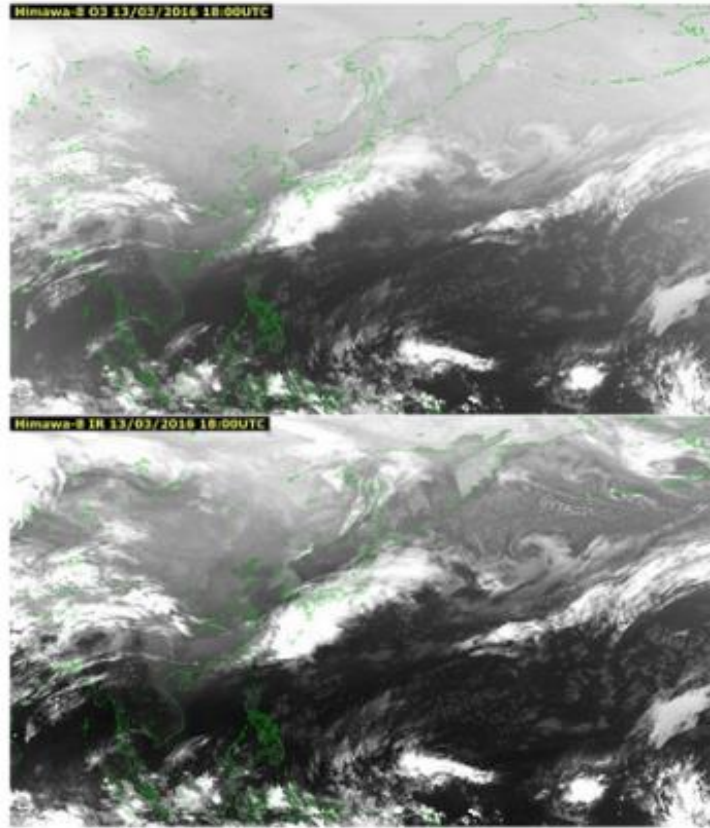


Fig. 1-2-38 Bands 12 (top) and 13 (bottom), with brightness temperature ranges of 220 to 300 K for both

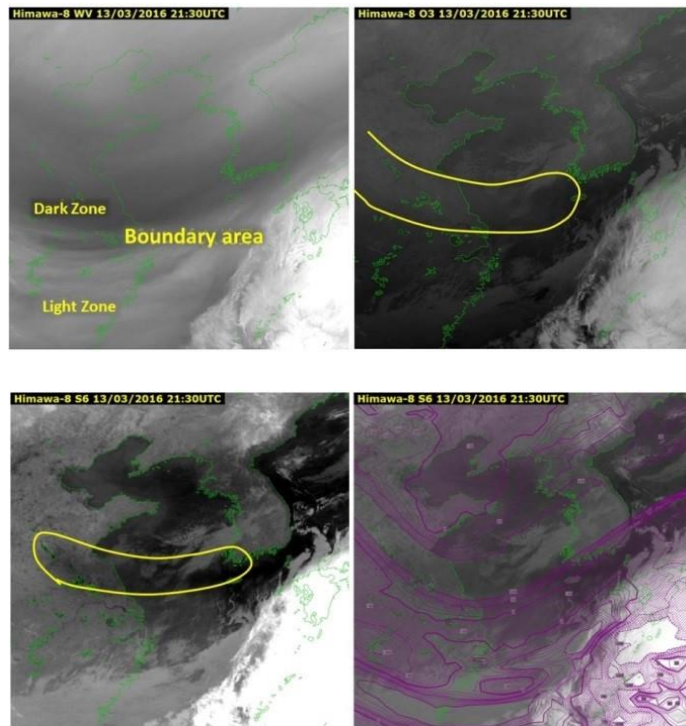


Fig. 1-2-39 White stripe in Band 12. Upper left: Band 8; upper right: Band 12; lower left: difference image between Bands 13 and 12; lower right: overlay of the same difference image and 300 hPa vorticity distribution from GSM (shading: negative vorticity).

N) Response to Silica in Volcanic Ash and Aeolian Dust (Band 15)

Since the emissivity of silica is larger in Band 15 than in Band 13, Band 15 imagery and difference imagery between the two can be used for detection of volcanic ash and Aeolian dust. This also applies to the emissivity of sand in Fig. 1-2-20. In Fig. 1-2-40, as seen from the correspondence with surface observation, the bright area in a difference image between Bands 13 and 15 corresponds to high concentrations of Aeolian dust.

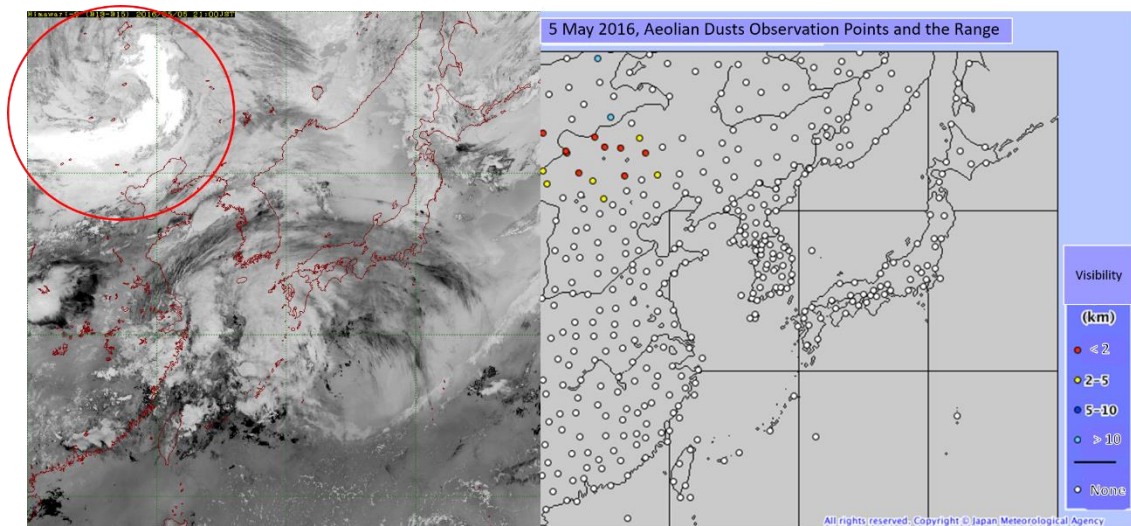


Fig. 1-2-40 Aeolian dust. The bright area within a red circle in the difference image between bands 13 and 15 (left) corresponds to high concentrations of Aeolian dust. The right panel shows surface observation of visibility at the same time (from the JMA website).

Figure 1-2-41 shows a volcanic eruption in Sakurajima in May 2016. The bright area in the difference image between Bands 13 and 15 corresponds to volcanic ash containing silica. The distinction between volcanic ash and upper clouds is much easier in the difference image than in the Band 3 image. Unlike Band 3 imagery, Band 15 imagery and related difference imagery applies to both day and night.

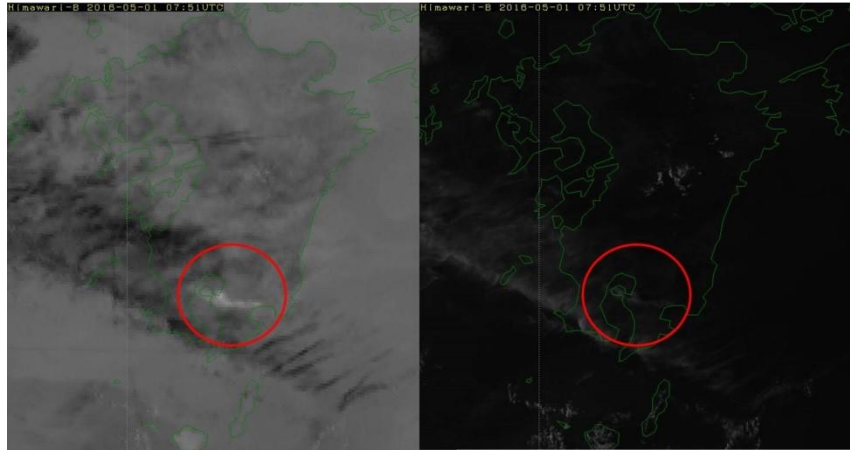


Fig. 1-2-41 Volcanic eruption in Sakurajima. Left: difference image between Bands 13 and 15; right: Band 3 image. The bright area on the left (red circle) corresponds to volcanic ash.

O) Response to Carbon Dioxide (Band 16)

As per Fig. 1-2-14, Band 16 is sensitive to absorption by carbon dioxide molecules. Accordingly, brightness temperatures in Band 16 are lower overall than in Band 13 (Fig. 1-2-42). Those in Band 16 are almost the same for thick clouds, but are much lower for lower clouds and cloudless sea surfaces (Fig. 1-2-43). This is because absorption by carbon dioxide in the lower atmosphere lowers the observed brightness temperature (Fig. 1-2-44).

It is difficult to estimate carbon dioxide distribution using only satellite imagery because temperature and water vapor distributions in the troposphere constantly change.

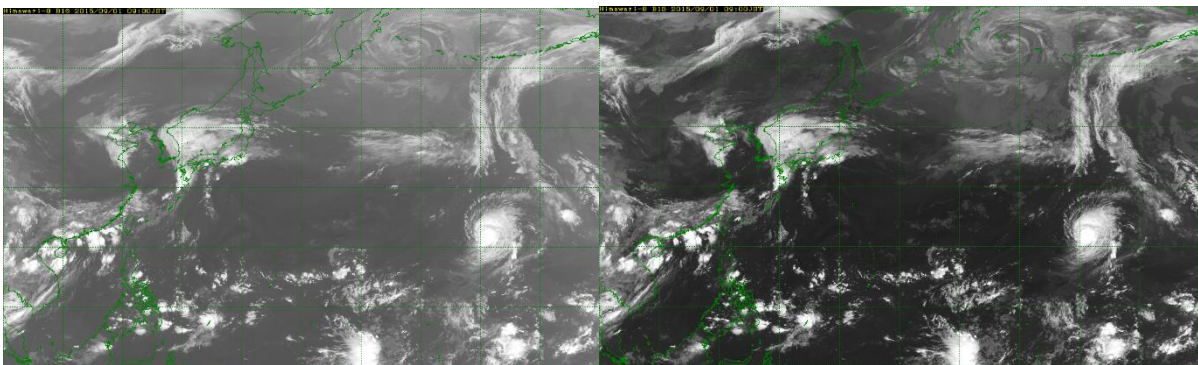


Fig. 1-2-42 Comparison of Bands 16 (top) and 13 (bottom) images. The brightness temperature range is 210 to 310 K for both.

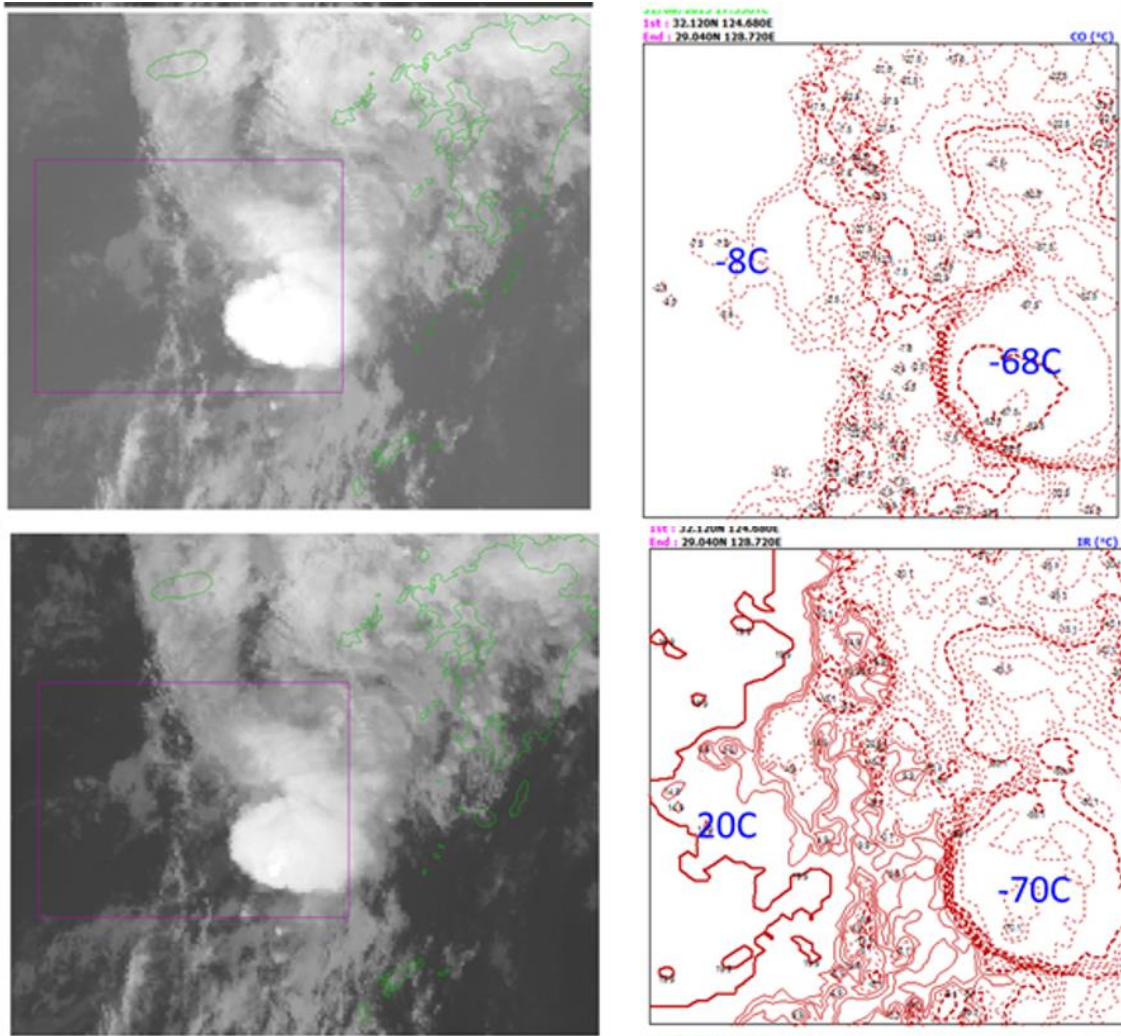


Fig. 1-2-43 Comparison of Bands 16 (top) and 13 (bottom). The right panels show brightness temperature distribution for the pink rectangle on the left.

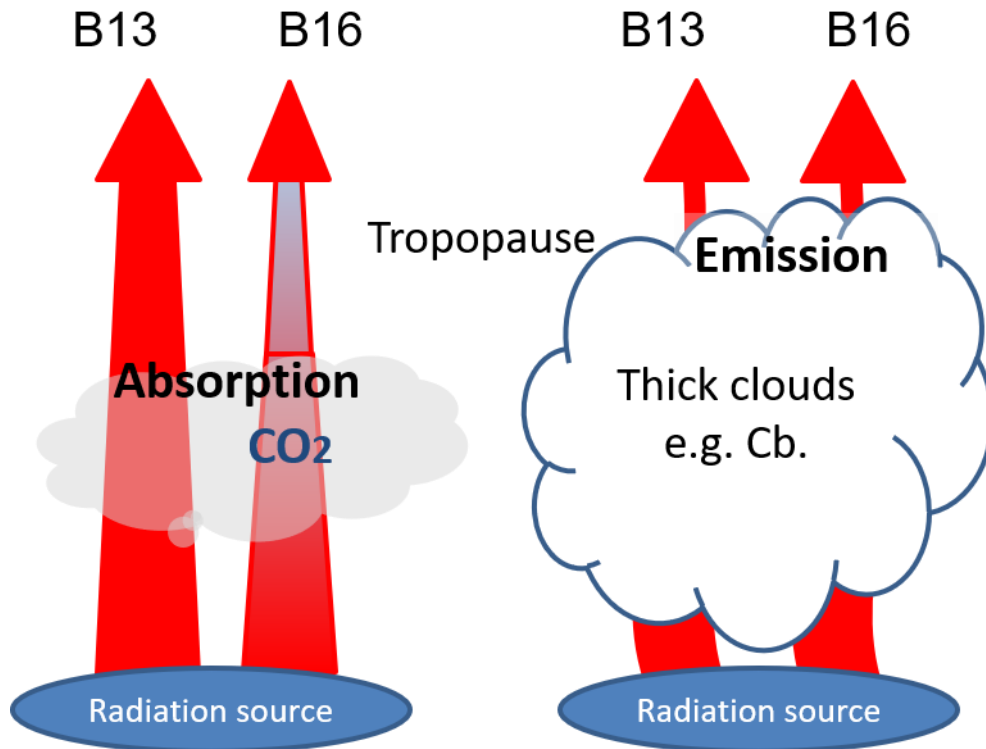


Fig. 1-2-44 Difference in radiance between Bands 13 and 16

#### (5) Infrared Band Characteristics

The characteristics of the bands described in this chapter are as below (values in parentheses: central wavelengths).

- Band 7 (3.9  $\mu\text{m}$ )
  - One of the window bands
  - The successor to IR4 on MTSAT-2
  - Used for hotspot detection
  - Significantly affected by sunlight reflection, with observed radiance containing both reflected sunlight and Earth radiation for the daytime
  - Reflected sunlight component sensitive to cloud particle phases
- Band 8 (6.2  $\mu\text{m}$ )
  - One of the water vapor bands
  - According to the weighting function, correspondence to the upper troposphere (the highest altitude among water vapor bands)
  - The successor to IR3 on MTSAT-2
- Band 9 (6.9  $\mu\text{m}$ )
  - One of the water vapor bands
  - According to the weighting function, correspondence to the upper to middle troposphere (slightly below Band 8)

## Utilization of Meteorological Satellite Data in Cloud Analysis

- Band 10 (7.3  $\mu\text{m}$ )
  - One of the water vapor bands
  - According to the weighting function, correspondence to the middle troposphere (the lowest altitude among water vapor bands)
  - Sensitive to sulfur dioxide and useful for monitoring volcanic gas
- Band 11 (8.6  $\mu\text{m}$ )
  - One of the window bands (more affected by atmospheric molecules than Bands 13 to 15)
  - Sensitive to cloud particle phases
  - Sensitive to sulfur dioxide and useful for monitoring volcanic gas
- Band 12 (9.6  $\mu\text{m}$ )
  - Sensitive to ozone
- Band 13 (10.4  $\mu\text{m}$ )
  - One of the window bands
  - The successor to IR1 on MTSAT-2.
  - Observation of radiation in the most transparent wavelength region (the closest transmittance to 1 among Bands 13 to 15; known as a clean window band)
- Band 14 (11.2  $\mu\text{m}$ )
  - One of the window bands
- Band 15 (12.4  $\mu\text{m}$ )
  - One of the window bands
  - The successor to IR2 on MTSAT-2
  - Observation radiation with the least transmittance among Bands 13 to 15 (known as a dirty window band)
  - Sensitive to cloud particle phases and useful for distinguishing especially thin upper clouds
  - Different characteristics from Band 13 for silica (abundant in volcanic ash and Aeolian dust)
- Band 16 (13.3  $\mu\text{m}$ )
  - Sensitive to carbon dioxide

### References:

- Clerbaux C., J. R. Drummond, J. Fland and J. Orphal, 2011: Remote Sensing of Tropospheric Composition from Space, <https://doi.org/10.1007/978-3-642-14791-3>
- Delst, P. van and Y. Han, 2008: CRTM Technical Subgroup Report, 2, available at [https://itwg.ssec.wisc.edu/wordpress/wp-content/uploads/2023/05/04\\_13\\_CRTMWG\\_itsc16.pdf](https://itwg.ssec.wisc.edu/wordpress/wp-content/uploads/2023/05/04_13_CRTMWG_itsc16.pdf)

## Chapter 1. Outline of Meteorological Satellite Observation

- Ellrod, G. P., 1995 : Advance in the Detection and Analysis of Fog at Night Using GOES Multispectral Infrared Imagery, *Weather and forecasting*, 10, 606-619.
- GOES-R Program Office (NOAA Satellite and Information Service), 2015-2016: ABI Bands Quick Information Guides, available at <http://www.goes-r.gov/education/ABI-bands-quick-info.html>
- Hayashi, M., 2018: Introduction to the Computation Method for Cloud Radiative Processes and Its Application for the Advanced Himawari Imager onboard Himawari-8, *Meteorological Satellite Center Technical Note*, No.63, 1-38 (Japanese).
- Kumabe, R. (ed.), 2006: Meteorology from satellites: on the uses of multi-channel data, *meteorological research notes*, No.212, 51 – 54 (Japanese).
- Li, J., C. C. Schmidt, J. P. Nelson, T. J. Schmit, and W. P. Menzel, 2001: Estimation of total atmospheric ozone from GOES sounder radiances with high temporal resolution, *Journal of Atmospheric and Oceanic Technology*, 18, 157-168, available at [https://doi.org/10.1175/1520-0426\(2001\)018<0157:EOTAOF>2.0.CO;2](https://doi.org/10.1175/1520-0426(2001)018<0157:EOTAOF>2.0.CO;2)
- Murata, H., M. Takahashi and Y. Kosaka, 2015: VIS and IR bands of Himawari-8/AHI compatible with those of MTSAT-2/Imager, *Meteorological Satellite Center technical note*, No.60, 1-18.
- MSC, 2000: “Analysis and usages of meteorological satellite imageries”, *General meteorology version*, 1 - 12 (Japanese).
- MSC, 2002: “Analysis and usages of meteorological satellite imageries”, *Aviation meteorology version*, 27 - 28 (Japanese).
- MSC, 2005: “Analysis and usages of meteorological satellite imageries”, *Analysis and Usages of 3.8 $\mu$ m version*, 23 - 24 (Japanese).
- Nakajima, T. and M. Tanaka, 1986: Matrix formulation for the transfer of solar radiation in a plane-parallel scattering atmosphere, *J. Quant. Spectrosc. Radiat. Transfer*, 35, 13-21.
- Nakajima, T. and M. Tanaka, 1988: Algorithms for radiative intensity calculations in moderately thick atmospheres using a truncation approximation, *J. Quant. Spectrosc. Radiat. Transfer*, 40, 51-69.
- Rosenfeld, D., 2004: Applications of Meteosat Second Generation (MSG) CONVERSION FROM COUNTS TO RADIANCES AND FROM RADIANCES TO BRIGHTNESS TEMPERATURES AND REFLECTANCES, available at <https://rammb.cira.colostate.edu/wmovl/vr1/pptlectures/eumetsat/PowerPoints/Channels/conversion.ppt>
- Schmetz, J., Y. Govaerts, K. Marianne, H. Lutz, A. Ratier and S. Tjemkes, 2004: A short introduction to METEOSAT Second Generation (MSG), 1-9, available at [http://www.eumetsat.int/website/wcm/idc/idcplg?IdcService=GET\\_FILE&dDocName=ZIP\\_MSG\\_GUIDE\\_C&RevisionSelectionMethod=LatestReleased&Rendition=Web](http://www.eumetsat.int/website/wcm/idc/idcplg?IdcService=GET_FILE&dDocName=ZIP_MSG_GUIDE_C&RevisionSelectionMethod=LatestReleased&Rendition=Web)
- Simizu, K., K. Saito, and M. Yamamoto, 2017: “Characteristics of imageries of AHI 16

- bands / Himawari-8”, MSC Technical Report No.62, 39 - 71 (Japanese).
- Stamnes, K., S.-C. Tsay, W. Wiscombe, and K. Jayaweera, 1988: Numerically stable algorithm for discrete-ordinate-method radiative transfer in multiple scattering and emitting layered media, Appl. Opt., 27, 2502-2509.
  - WMO, 2007: RGB composite satellite imagery workshop final report (5-6 JUNE 2007 Boulder, CO, U.S.A.), available at [http://www.wmo.int/pages/prog/sat/documents/RGB-1\\_Final-Report.pdf](http://www.wmo.int/pages/prog/sat/documents/RGB-1_Final-Report.pdf)
  - WMO, 2012: WMO/EUMETSAT workshop on RGB satellite products final report (17-19 SEPTEMBER 2012, Seeheim, Germany), available at [http://www.wmo.int/pages/prog/sat/documents/RGB-WS-2012\\_FinalReport.pdf](http://www.wmo.int/pages/prog/sat/documents/RGB-WS-2012_FinalReport.pdf)
  - Yokota, H. and M. Sasaki, 2013: “Introduction to geostationary earth environment observation satellite “Himawari8 and 9””, MSC Technical Report, No.58, 121-138 (Japanese).
  - Zwatz-Meise, V., 2004: Introduction into the Absorption Channels: Description of characteristics and content of the Ozone channel: Ch08: 9.7, 12-27, available at [http://oiswww.eumetsat.org/WEBOPS/msg\\_interpretation/PowerPoints/Channels/O3guide.ppt](http://oiswww.eumetsat.org/WEBOPS/msg_interpretation/PowerPoints/Channels/O3guide.ppt)

Websites:

- JMA homepage  
(Observation examples of Himawari)  
<http://www.jma-net.go.jp/sat/himawari/image.html> (Japanese)  
(The world distribution map of monthly average of total ozone volume)  
[http://www.data.jma.go.jp/gmd/env/ozonehp/totozone\\_glbsat\\_monthave.html](http://www.data.jma.go.jp/gmd/env/ozonehp/totozone_glbsat_monthave.html) (Japanese)  
(Aeolian dust distribution)  
<http://www.jma.go.jp/en/kosa/>
- JMA/MS  
(Himawari-8/9 Operational Information)  
<http://www.data.jma.go.jp/mscweb/en/operation8/index.html>  
<http://www.jma-net.go.jp/msc/en/index.html>
- NASA  
Spectral Response Function Database  
<https://www-pm.larc.nasa.gov/cgi-bin/site/showdoc?mnemonic=SPECTRAL-RESPONSE>

### 1.3. Imagery Comparison

In this section, the imagery characteristics described above are separated into day and night for clarification with specific examples. Table 1-3-1 lists the relevant imagery types and related transition. In difference imagery for Band 13 and Band 15 (referred to here as B13-B15) and for Band 7 and Band 13 (B07-B13), larger differences appear darker and smaller differences appear lighter.

Table 1-3-1. Imagery appearance

Types	Imagery appearance				
	White	Light grey	Grey	Dark grey	Black
Visible (B03)	←	High reflectance		High reflectance	→
Near-infrared (B04, 05)	←	Low reflectance		Low reflectance	→
Water vapors (B08, 09, 10)	←	Wet		Dry	→
Infrared (B13)	←	Low temperature		High temperature	→
B13-B15	←	Negative		Positive	→
B13-B07	←	Negative		Positive	→

#### 1.3.1. Daytime Imagery

This section compares visible (Fig. 1-3-1), near-infrared (Fig. 1-3-2), water vapor (Fig. 1-3-3), infrared (Fig. 1-3-4) and infrared difference (B13-B15, Fig. 1-3-5) image from 03:00 UTC (12:00 JST) on 7 March 2016.

In visible imagery, cloud area A above the eastern sea off Amami Island is shown as a bulky cluster along with cloud area B. It has a streaky appearance and lower density than in B. The temperature is slightly higher (dark grey) in infrared imagery and related reflectance is higher (white) in near-infrared imagery for sensitivity to cloud particles in the water phase, indicating that the area is underdeveloped convective cloud (Cu).

The temperature of cloud area B is slightly lower (light grey) than in cloud area A, showing lower reflectance (grey) in near-infrared imagery. This is assumed to be an area of convective cloud containing cumulus congestus (Cg) with a higher top than the Cu of cloud area A.

Cloud area C can be judged as convective containing Cb. This is based on the overall thicker appearance in visible imagery, the lower temperature (white) than the surrounding cloud area in infrared imagery, and the display of cloud with lower reflectance (grey) in near-infrared imagery. The area is also bright in water vapor imagery and grey with little temperature difference in infrared difference imagery.

The temperature of cloud area D is low (white) in infrared imagery, with large reflectance (white) in visible imagery and low reflectance (dark grey) in near-infrared imagery, indicating a thick cloud area with a high top. Cloud area E has a lower temperature than D (white – light grey) in infrared imagery as well as being darker in visible imagery and having lower reflectance (dark grey) in infrared imagery, suggesting thin Ci. The appearance in water vapor imagery is similar to that of infrared imagery, although with obscurity at the edge of the cloud area. In infrared difference imagery, a minor temperature difference (light grey) is seen in association with cloud area D. A large temperature difference (black) is indicated for cloud area E, which appears to be thin Ci.

Region F is white in visible imagery, grey in infrared imagery and white in near-infrared imagery, altogether indicating an area with lower cloud. The smoothness of the cloud top surface with the same color tone as in visible/near-infrared imagery suggests a lower cloud area containing fog.

Region G is grey in visible/near-infrared imagery and white in infrared difference imagery. This corresponds to the region of Aeolian dust described in Section 1.2.

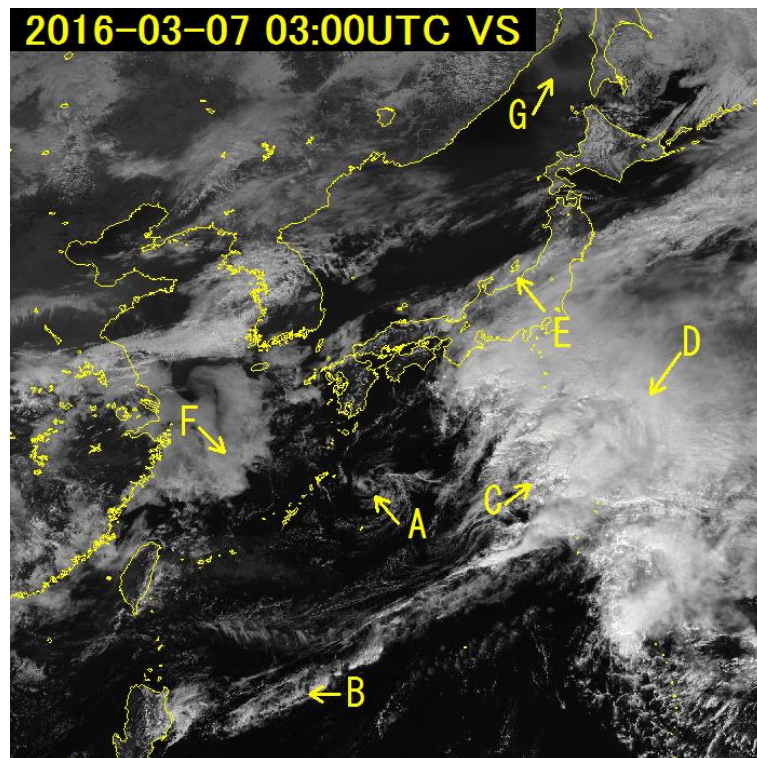


Fig. 1-3-1. B03 visible image for 03:00 UTC on 7 March 2016

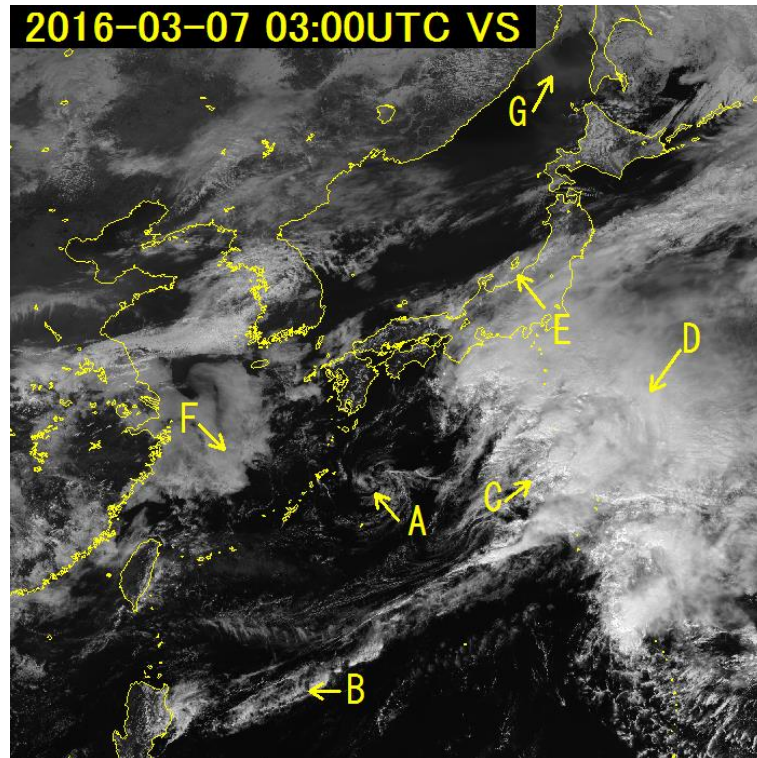


Fig. 1-3-2. B13 infrared image for 03:00 UTC on 7 March 2016

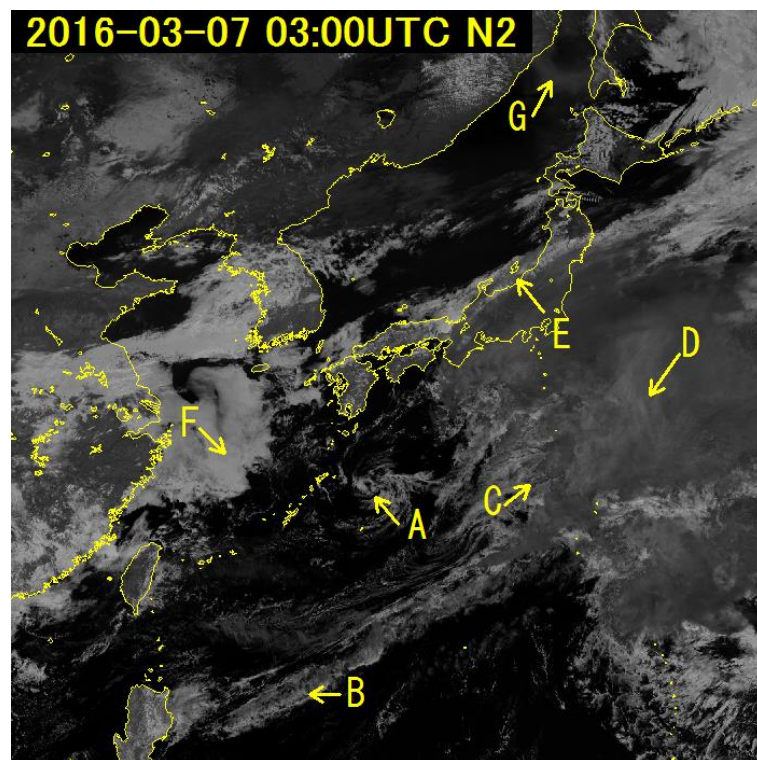


Fig. 1-3-3. B05 near-infrared image for 03:00 UTC on 7 March 2016

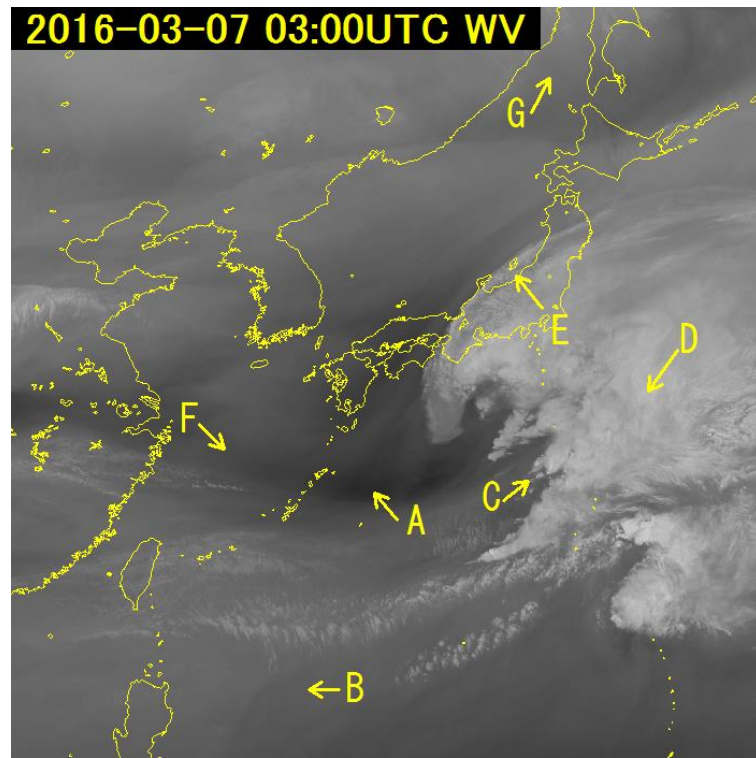


Fig. 1-3-4. B08 water vapor image for 03:00 UTC on 7 March 2016

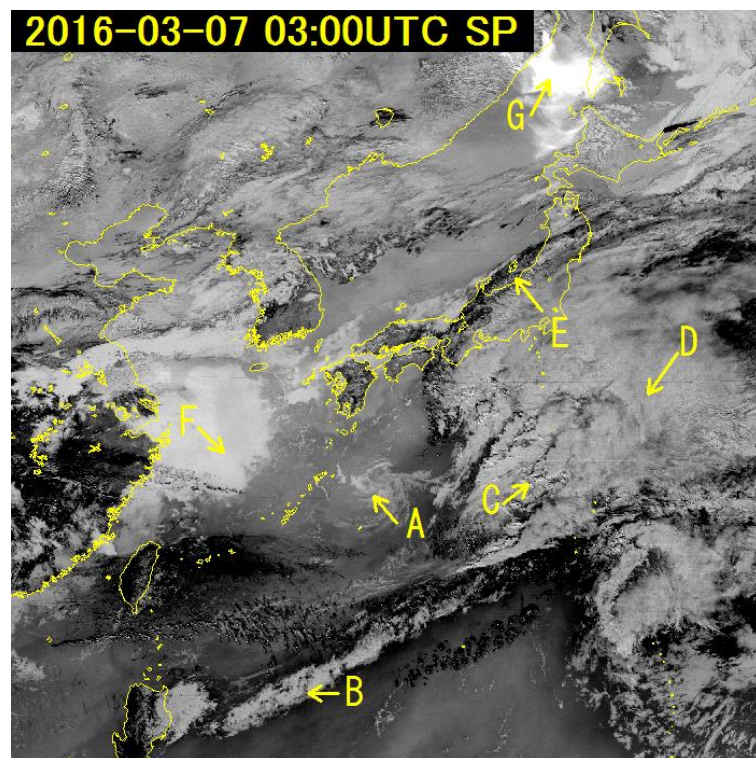


Fig. 1-3-5. B13-B15 infrared difference image for 03:00 UTC on 7 March 2016

### 1.3.2. Nighttime Imagery

In this section, B13 infrared (Fig. 1-3-6) imagery from 18:00 UTC on 6 March 2016 (03:00 JST on 7 March) is compared with difference image for B13-15 (Fig. 1-3-7) and B07-B13 (Fig. 1-3-8).

In Region A, a bright area is seen only in B13-B15. This corresponds to the region of Aeolian dust mentioned in the previous section. It is not seen in infrared imagery.

Region B shows a bright area in infrared imagery that displays as dark in the two difference images. As discussed above, this region corresponds to thin upper clouds. Identifying upper cloud areas is more difficult with infrared imagery; however, the B07-B03 image shows a thin upper cloud area in black since radiation from the lower layer is transmitted through it, making it easily distinguishable.

In Region C, the area is bright in infrared imagery, grey in B13-B15, and dotted in B07-B13. These correspond to an area of thick cloud with a high top, such as cumulonimbus. These areas are in a region at the front of two cyclones to the south of Japan.

Region D shows lower cloud in white/light grey in B07-B13 and grey in infrared imagery. As seen in Fig. 1-3-9, fog/mist is seen at many observation areas between northern Kyushu and the Tsushima Strait, indicating that D is a lower-cloud area containing fog.

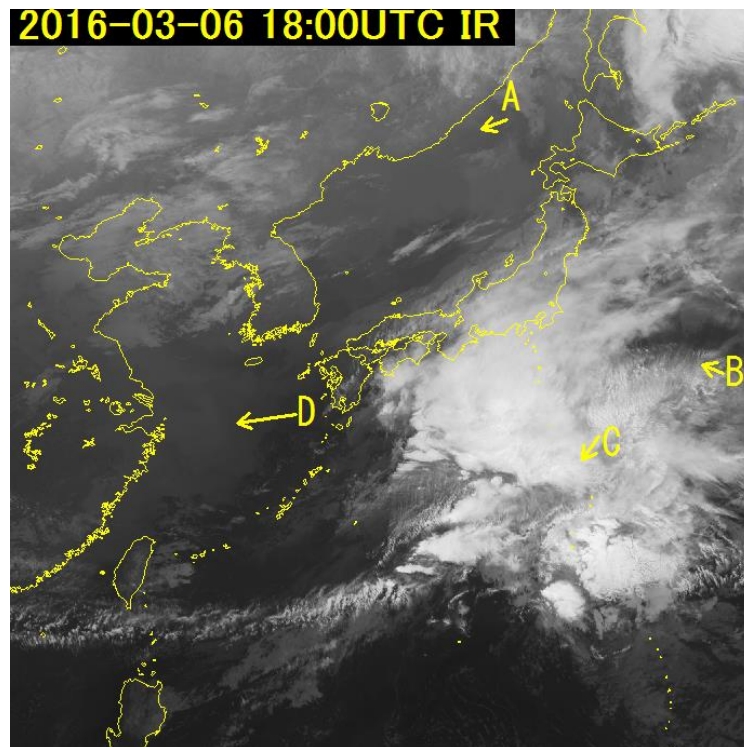


Fig. 1-3-6. B13 infrared image for 18:00 UTC on 6 March 2016

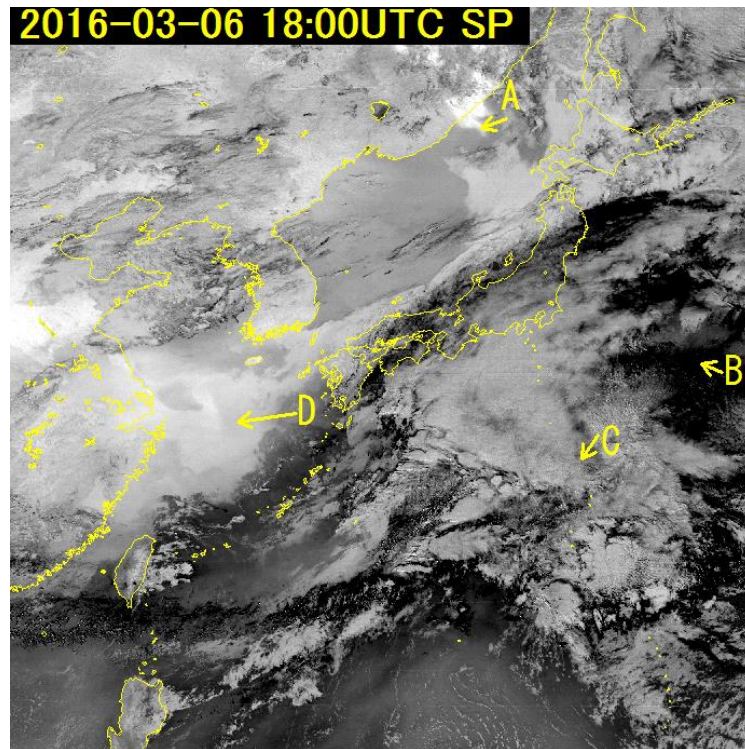


Fig. 1-3-7. B13-B15 infrared difference image for 18:00 UTC on 6 March 2016

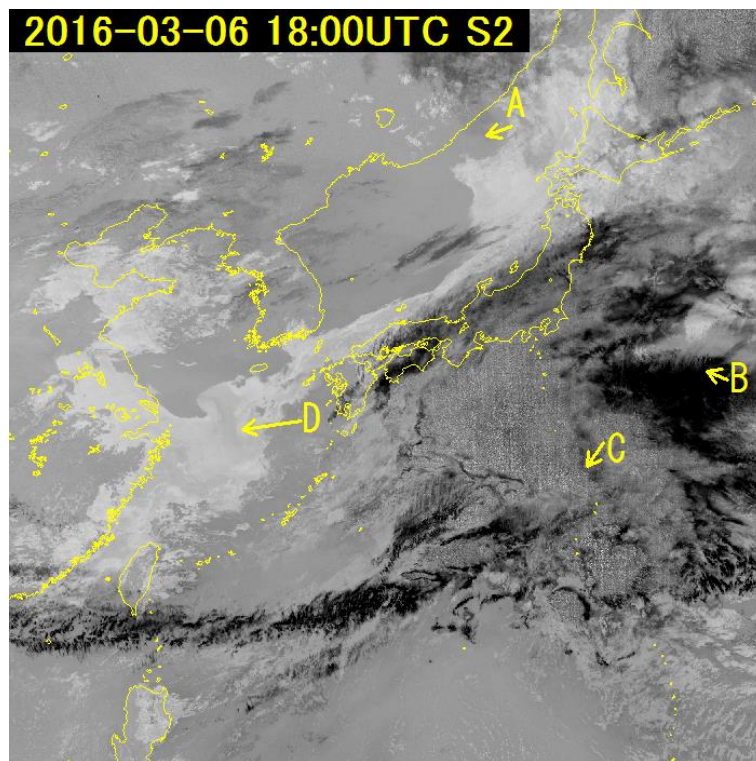


Fig. 1-3-8. B07-B13 infrared difference image for 18:00 UTC on 6 March 2016

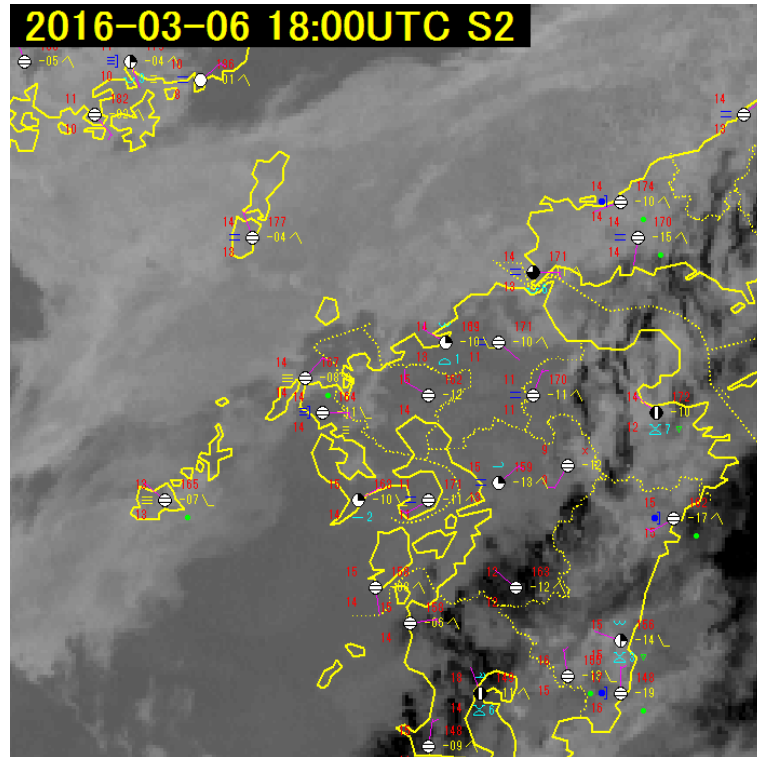


Fig. 1-3-9. B07-B13 infrared difference image for 18:00 UTC on 6 March 2016 based on surface meteorological observation

#### 1.4. RGB Composite Imagery

##### 1.4.1. Principles of RGB Composite Imagery

RGB (red, green, blue) composites display satellite imagery with overlays in combinations of the three primary colors (Fig. 1-4-1).

This technique makes identification of cloud areas and obscure phenomena easier than with simpler imagery based on bands or differences. However, variables such as latitude, seasonal conditions and the characteristics of satellite-mounted radiometers may require display outside the range of standard tones, making assessment based solely on color hues more difficult in certain cases. Accordingly, it is important to fully comprehend the characteristics of the bands used in compositions.

For clarity, the global standard for RGB composite imagery has been proposed by the WMO's RGB Composite Satellite Imagery Workshop.

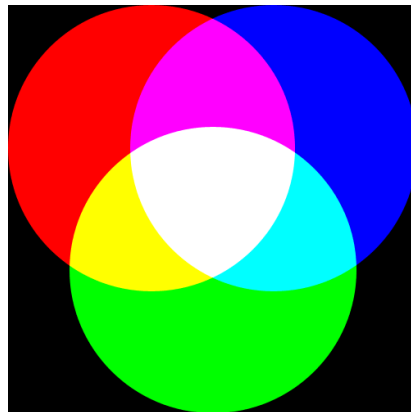


Fig. 1-4-1. RGB light combinations

##### 1.4.2. RGB Composite Imagery Characteristics

This section describes WMO-standard RGB composite image from 03:00 UTC on 7 March 2016 and 18:00 UTC on 6 March 2016. The relevant phenomena may not appear with the exact precision of the colors indicated above.

###### (1) True Color RGB

Figure 1-4-2 shows an overlay of visible imagery from Band 3 (0.64  $\mu\text{m}$ ), Band 2 (0.51  $\mu\text{m}$ ) and Band 1 (0.47  $\mu\text{m}$ ) bordered in red, green and blue, respectively, producing a display similar to that seen by the human eye. It is provided on the Visible (Color) Channel in Satellite Imagery (Rapid Scan) on the JMA website. These composites have the following characteristics:

- Display of cloud and snow/ice in white for ease of discrimination from land
- Facilitated viewing of smoke, Aeolian dust (yellow sand), volcanic ash and other forms of dust (Fig. 1-4-2)
- Exclusive daytime use due to application of visible imagery

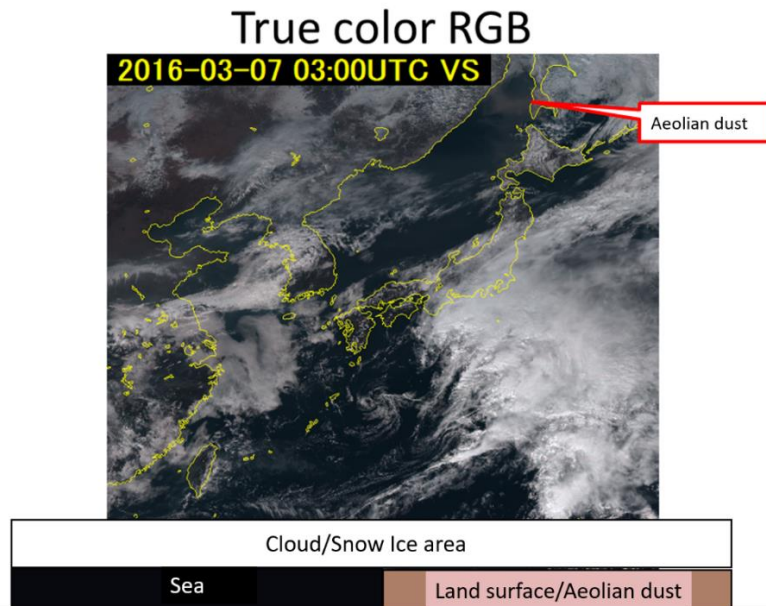


Fig. 1-4-2. True Color RGB sample

(2) Natural Color RGB

Figure 1-4-3 shows an overlay of visible image from Band 5 (1.6  $\mu\text{m}$ ), Band 4 (0.86  $\mu\text{m}$ ) and Band 3 (0.64  $\mu\text{m}$ ) bordered in red, green and blue, respectively, with the following characteristics:

- Band 5 (red) lower reflectance to ice crystals, resulting in regions of upper clouds and snow/ice appearing in cyan in composites of Band 4 (green) and Band 3 (blue) with higher reflectance (Fig. 1-4-4)
- High reflectance to water droplets in all three bands, causing droplet-based cloud areas (e.g., fog and low clouds) to appear in a white tone composed of the three primary colors
- Especially high Band 4 (green) reflectance against vegetation in comparison to the other two bands, causing vegetation to appear in green
- Exclusive daytime use due to application of visible and near-infrared image

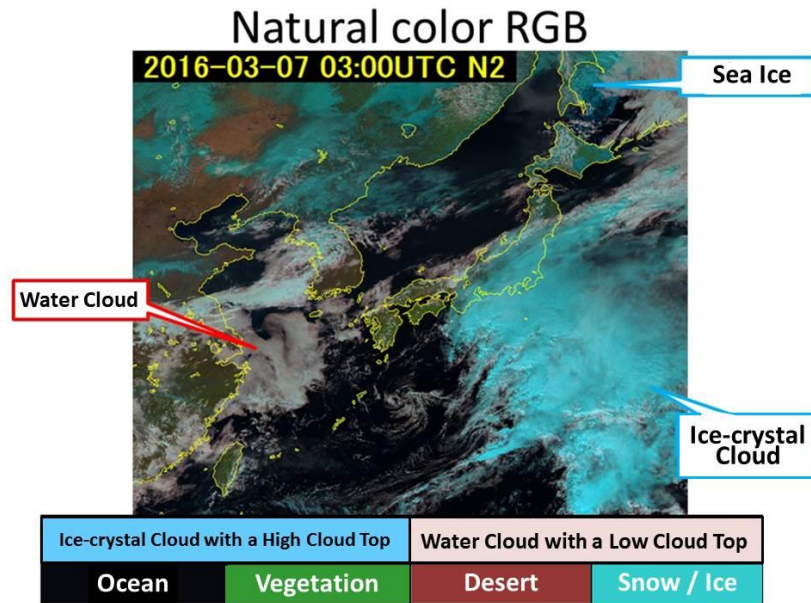


Fig. 1-4-3. Natural Color RGB sample

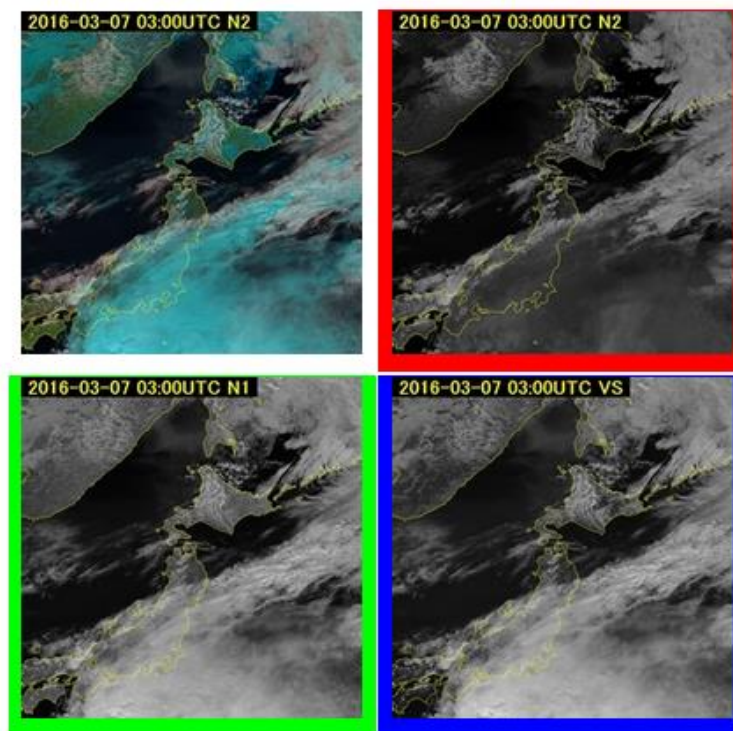


Fig. 1-4-4. Natural Color RGB composite image (top left) and source image. Top right: Band 5; bottom left: Band 4; bottom right: Band 3

(3) Dust RGB

Figure 1-4-5 shows difference image from Band 15 and Band 13 (referred to here as B15-B13), Band 13 and Band 11 (B13-B11), and contrast-inverted image (i.e., adjusted to appear in color transition with higher brightness temperature) from Band 13 overlaid with red, green and blue (B13-inverted).

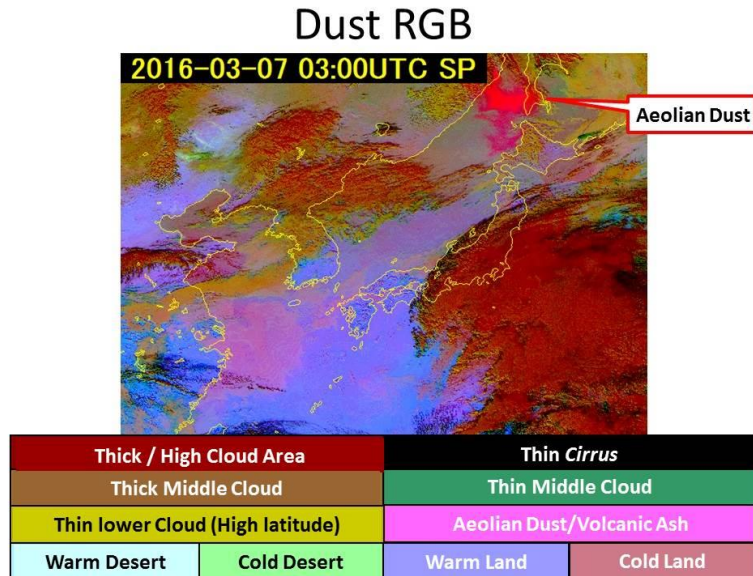


Fig. 1-4-5. Dust RGB color sample

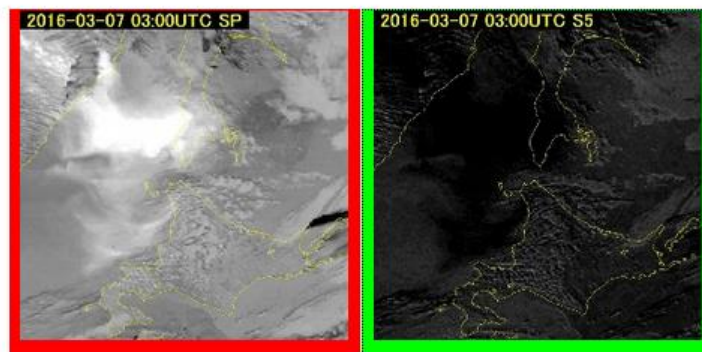


Fig. 1-4-6. Difference images used in Dust RGB composites. Left: B15-B13 showing Aeolian dust and volcanic ash in clear white; right: B13-B11 with Aeolian dust and volcanic ash in black

Dust RGB imagery has the following characteristics:

- Aeolian dust brighter in B15-B13 (Fig. 1-4-6: Left) and darker in B13-B11 (Fig. 1-4-6: Right); enhanced red in the former, with Aeolian dust and volcanic ash in magenta (Fig. 1-4-5)
- Capacity for alteration of display transition and gamma values to create Ash RGB imagery for enhanced visibility of volcanic ash and 24-hour Microphysics RGB imagery to facilitate cloud discrimination
- 24-hour applicability due to the absence of visible and near-infrared band data

(4) Airmass RGB

Figure 1-4-7 shows an overlay of difference image for Band 10 (7.3  $\mu\text{m}$ ) and Band 8 (6.2  $\mu\text{m}$ ) (referred to here as B10-B08), Band 13 (10.4  $\mu\text{m}$ ) and Band 12 (9.6  $\mu\text{m}$ ) (B13-B12) and Band 8

(6.2  $\mu\text{m}$ ) bordered in red, green, and blue, respectively, with the following characteristics:

- Brighter upper-middle atmosphere (dry or wet throughout) in B10-B08 (Fig. 1-4-8 right)
- Transition adjusted in B13-B12 to display the polar side darker and the sub-tropical high side brighter (Fig. 1-4-8 left).

Based on these characteristics, air masses and the jet stream axis can be approximated in Airmass RGB composites (Fig. 1-4-7). 24-hour application is also possible due to the absence of data from visible and near-infrared bands.

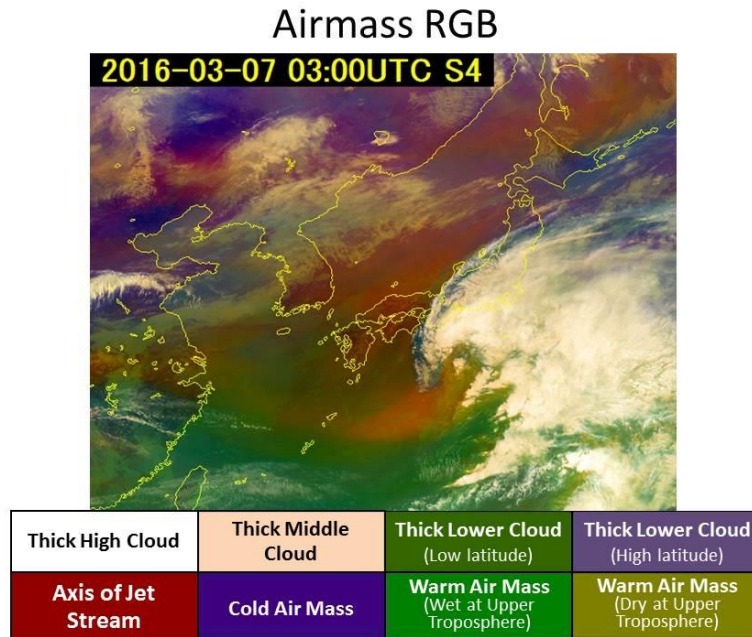


Fig. 1-4-7. Airmass RGB color sample

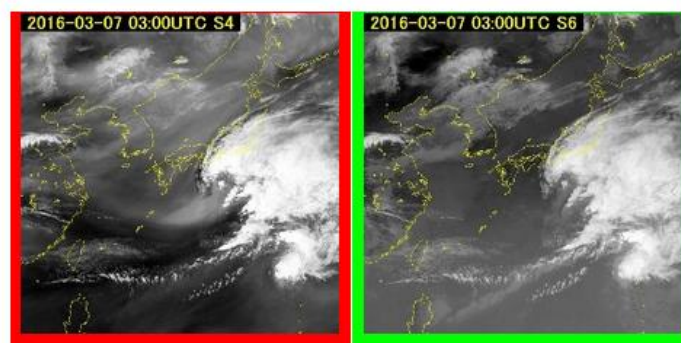


Fig. 1-4-8. Difference images used for Airmass RGB compositing. Left: B08-B10; right: B13-B12

(5) Night Microphysics RGB

B15-B13, B13-B07 and B13-inverted are bordered in red, green, and blue, respectively in Fig. 1-4-9. Night Microphysics RGB image has the following characteristics:

- Brighter fog/low cloud areas in all three types (in white with traces of green) (Fig. 1-4-

10)

- Poor resolution in Band 7 for lower-temperature regions; increased noise in B13-B07, causing yellow dots to appear in thick high-top cloud areas such as cumulonimbus (Fig. 1-4-10)
- Exclusivity to nighttime usage to avoid Band 7 sunlight influence

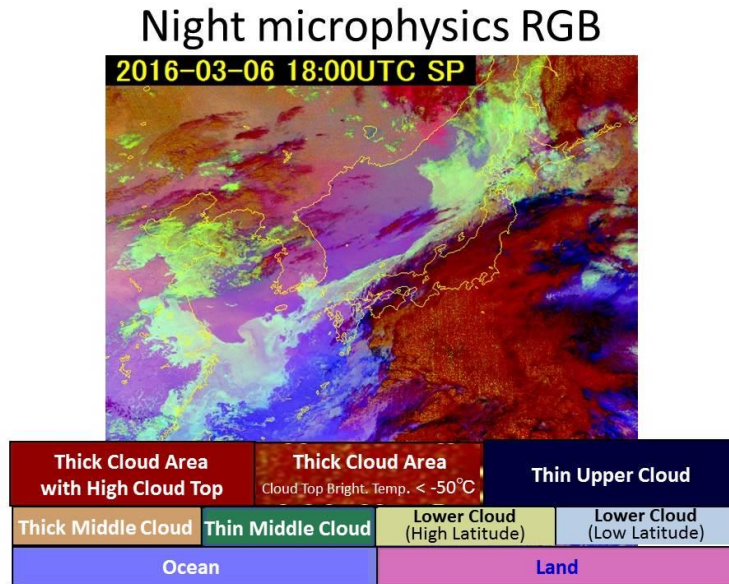


Fig. 1-4-9. Night Microphysics RGB sample

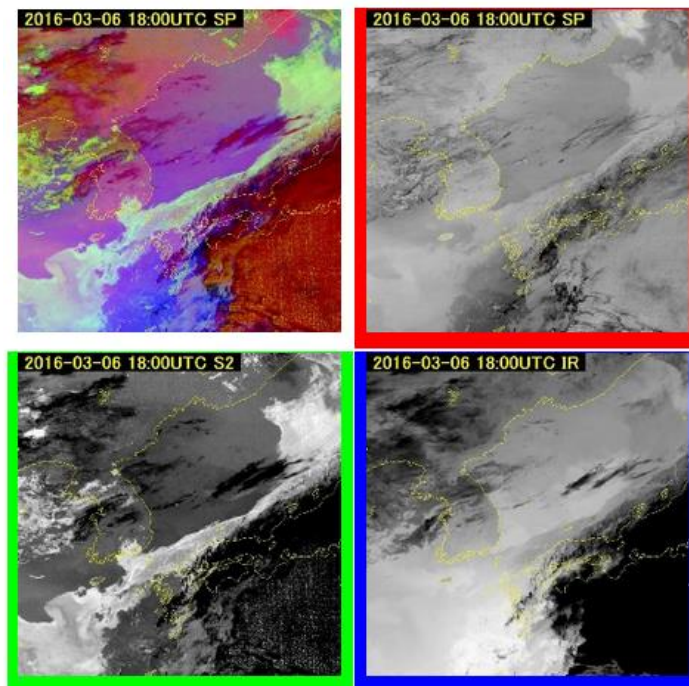


Fig. 1-4-10. Night Microphysics composite imagery (top left) and source images. Top right: B15-B13; bottom left: B13-B07; bottom right: B13-inverted

(6) Day Convection Storm RGB

Figure 1-4-11 shows difference image for Band 1 and Band 8 (referred to here as B10-B08),

Band 7 and Band 13 (B07-B13) and Band 5 and Band 3 (B05-B03) bordered in red, green and blue, respectively. Day Convection Storm RGB composite imagery has the following characteristics:

- Cloud particles brought up to the cloud top by strong updrafts faster, even before particle development, in cloud areas with extreme phenomena such as gusting winds and tornadoes, resulting in the formation of small ice crystals at the cloud top in areas with active convection. Cloud areas are notably brighter in B07-B13 and B10-B08 and darker in B05-B03 (displayed in yellow in composite image) (Fig. 1-4-12).
- Exclusive to daytime applicability due to the use of visible and near-infrared imagesy

### Day Convective Storms RGB

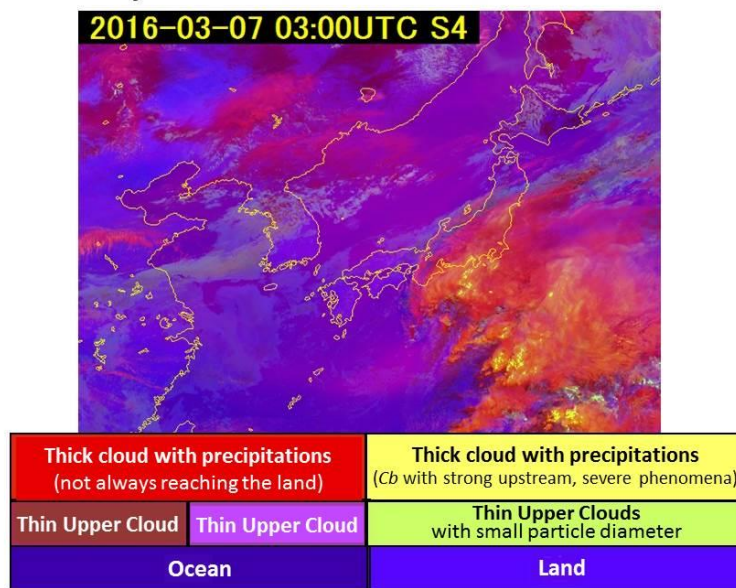


Fig. 1-4-11. Day Convective Storm RGB sample

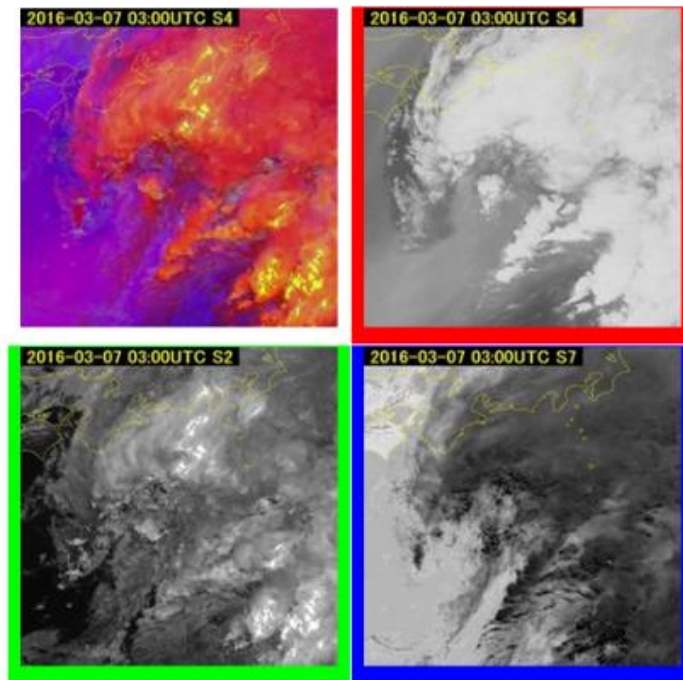


Fig. 1-4-12. Composite image for Day Convective Storm RGB (top left) and source images.

Upper right: B10-B08; lower left: B07-B13; lower right: B05-B03

## 2. RGB Composite Imagery Comparison

### (1) Infrared Imagery

In Fig. 1-4-13, a cloud area in front of a cyclone toward the south of Japan appears bright (a), mainly having Cb and Ci with high cloud tops. In contrast, cloud areas (b), (d) and (a) between the Korean Peninsula and the continent are dark. These are assumed to have lower cloud tops than (a).

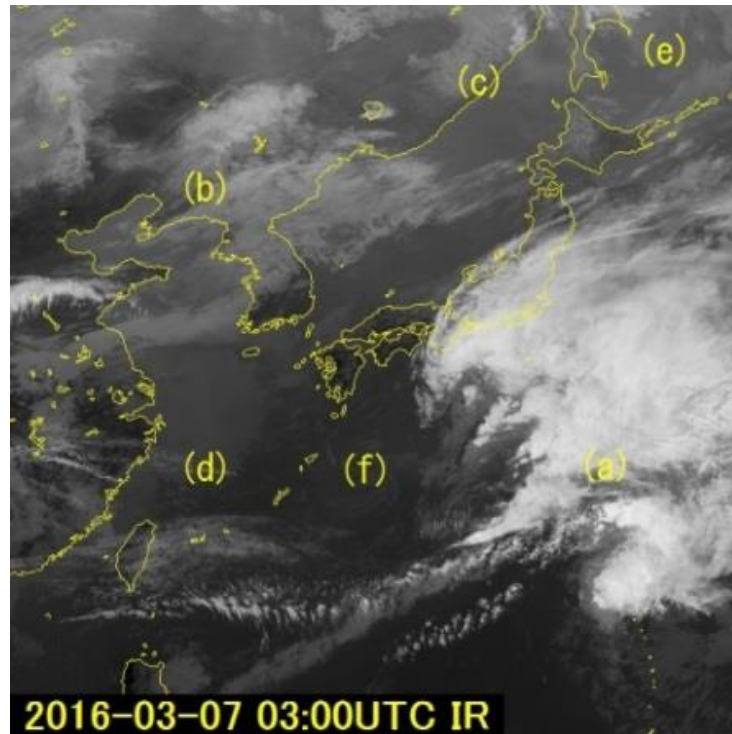


Fig. 1-4-13. Infrared image for 03:00 UTC on 7 March 2016

(2) True Color RGC Composite Imagery

In Fig. 1-4-14, the cloud area (a) appears bright, consisting mainly of thick clouds. Aeolian dust (c) is seen in brown between Hokkaido and Siberia. The cloud area (d) appears smooth on its surface; the obscurity in (a) indicates the presence of fog or low cloud. In (2), sea ice and cloud areas are visible, but are difficult to distinguish from this image alone.

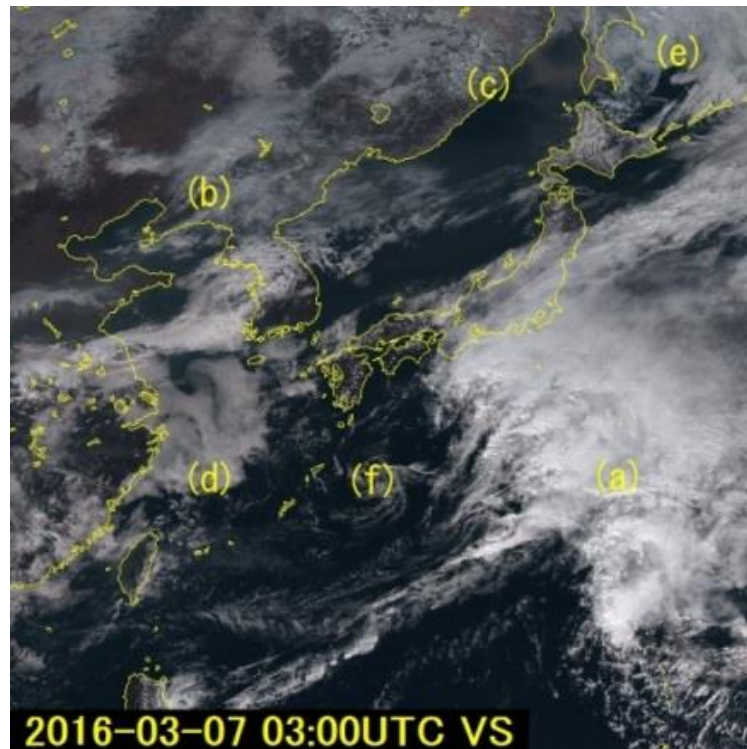


Fig. 1-4-14. True Color RGB composite image for 03:00 UTC on 7 March 2016

### (3) Natural Color RGB Composite Imagery

In Fig. 1-4-15, the cloud areas (d) in white and (a) in cyan are easily distinguishable. Aeolian dust (c) is shown thinner than in True Color; ground surface ice/seawater is in cyan and low cloud is in white, also facilitating identification. However, in (b), upper cloud and ice/sea ice areas are both in cyan. Accordingly, infrared imagery comparison and checking of multiple images are crucial in related discrimination.

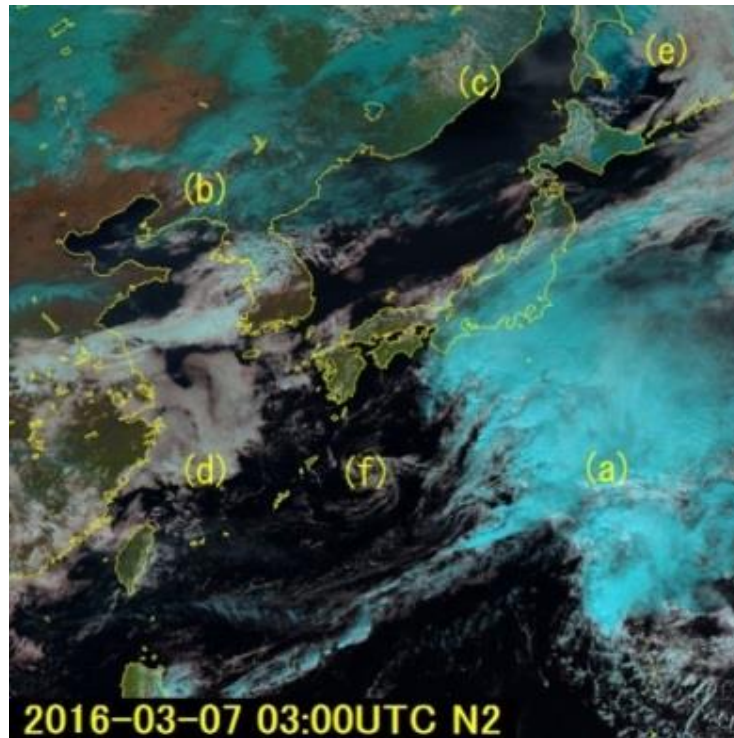


Fig. 1-4-15. Natural Color RGB composite image for 03:00 UTC on 7 March 2016

(4) Dust RGB Composite Imagery

In Fig. 1-4-16, Aeolian dust (c) is displayed in magenta, enabling easier identification than in B and C.

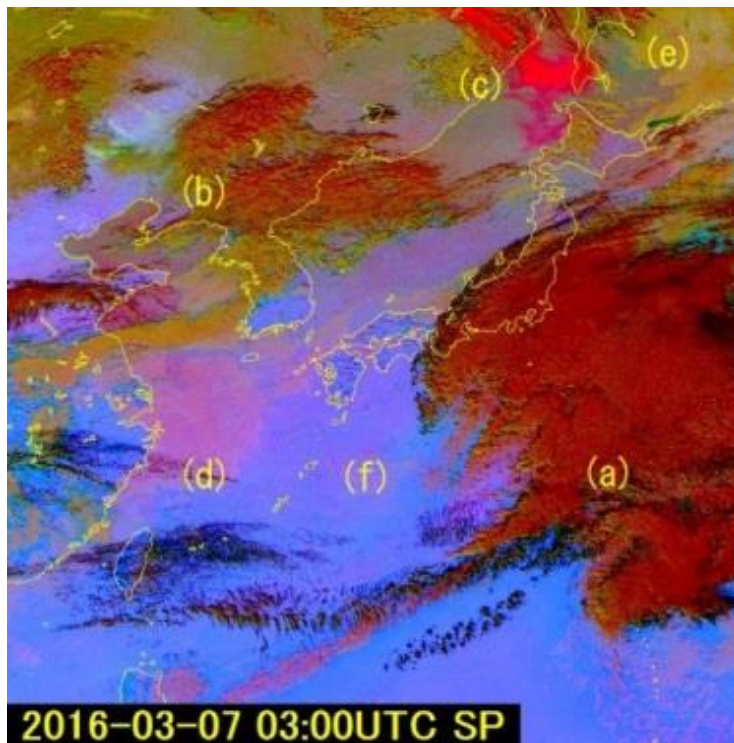


Fig. 1-4-16. Dust RGB composite image for 03:00 UTC on 7 March 2016

(5) Airmass RGB Composite Imagery

In Fig. 1-4-17, high cloud top areas such as (a) are shown in white. Orange indicates the presence of dry air or the jet stream axis. Here, the orange in (d) and (f) corresponds to the jet stream axis shown on the upper-level weather chart H throughout (b), (c) and (e), and an area of depression corresponding to the trough shown as H on the weather chart (Fig. 1-4-20).

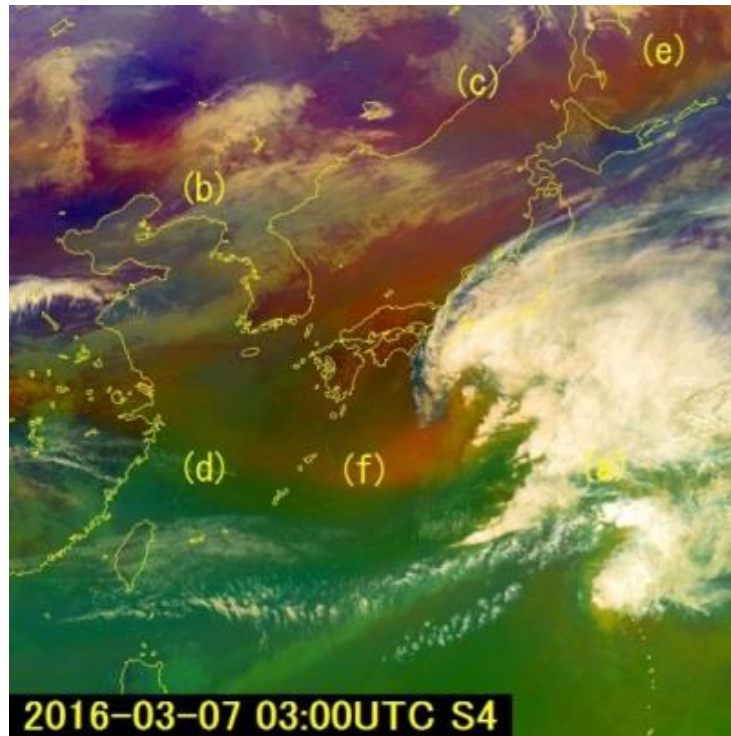


Fig. 1-4-17. Airmass RGB composite image for 03:00 UTC on 7 March 2016

(6) Day Convective Storm RGB Composite Imagery

In Fig. 1-4-18, particularly active convection in the cloud area (a) is shown in yellow. The B08-B10 difference image used here shows an area of depression corresponding to the trough of (d) and (f) in magenta.

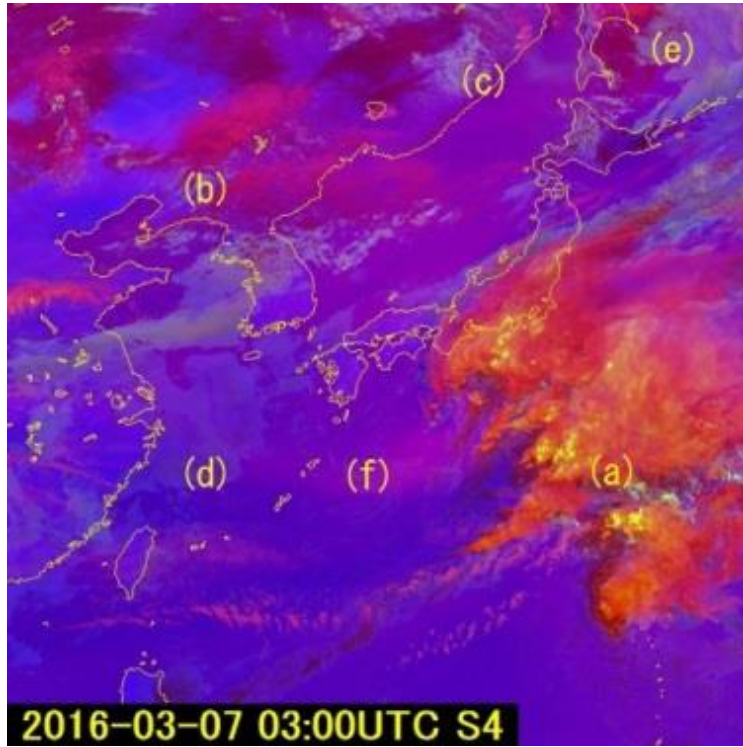


Fig. 1-4-18. Day Convective Storm RGB composite image

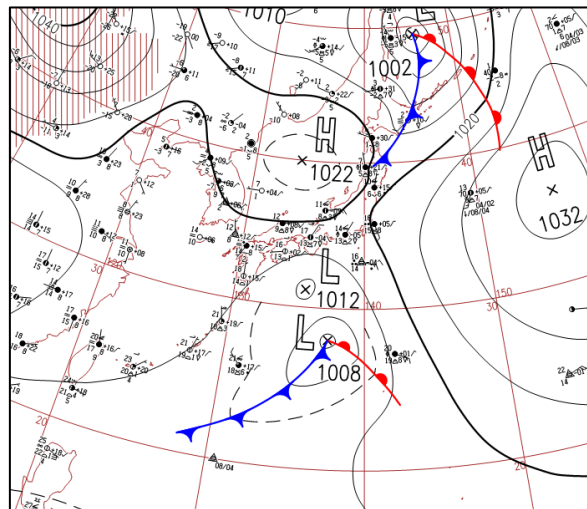


Fig. 1-4-19. Weather chart prompt report for 00:00 UTC on 7 March 2016

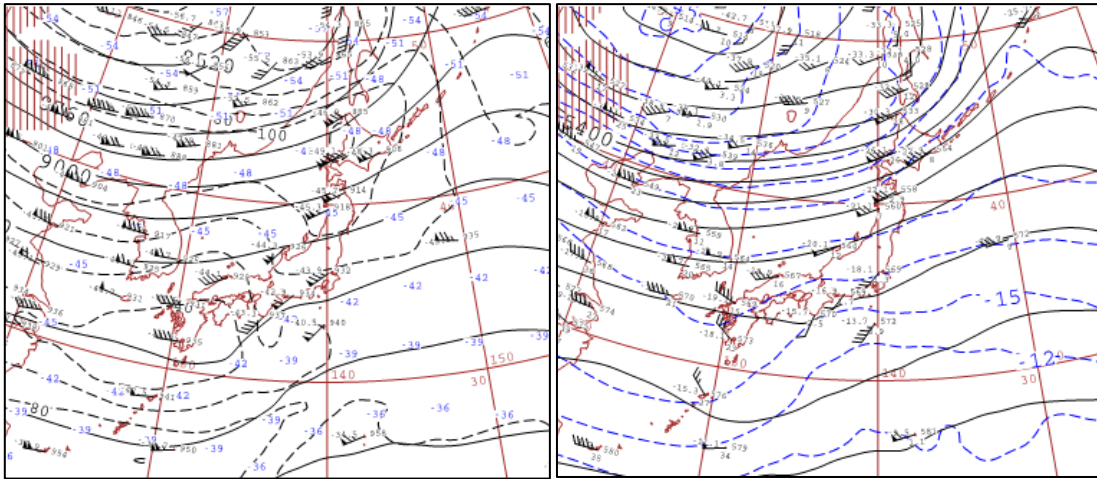


Fig. 1-4-20. Upper-level weather chart for 00:00 UTC on 7 March 2016. Left: 300 hPa; right: 500 hPa

Nighttime RGB composite images are compared below. For reference, a weather chart prompt report for the same time period is shown (Fig. 1-4-19 and 1-4-20).

(7) B13 Infrared Imagery (Nighttime)

The cloud area (a) appears brighter in front of a cyclone to the south of Japan, indicating the presence of Cb and Ci with higher cloud top as its main body (Fig. 1-4-21). The cloud area (b) over the Korean Peninsula and the continent is darker, indicating a lower cloud top than in (a).

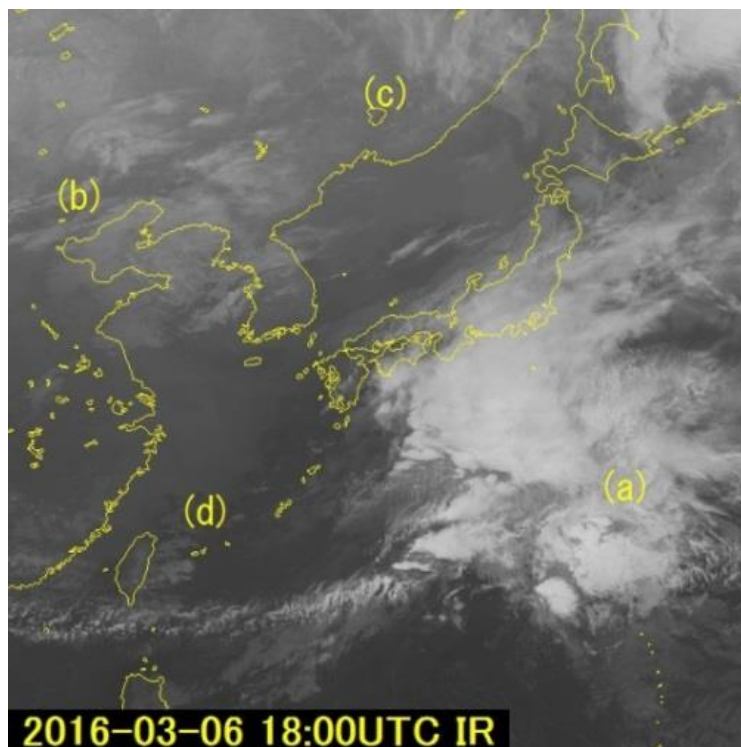


Fig. 1-4-21. B13 Infrared image for 18:00 UTC on 6 March 2016

(8) Dust RGB Composite Imagery (Nighttime)

The region (c) corresponding to Aeolian dust over Russia and China is clearly highlighted in magenta. The cloud area (a) appears in dark orange (Fig. 1-4-22). The cloud area (b) is difficult to identify due to its display in the same color.

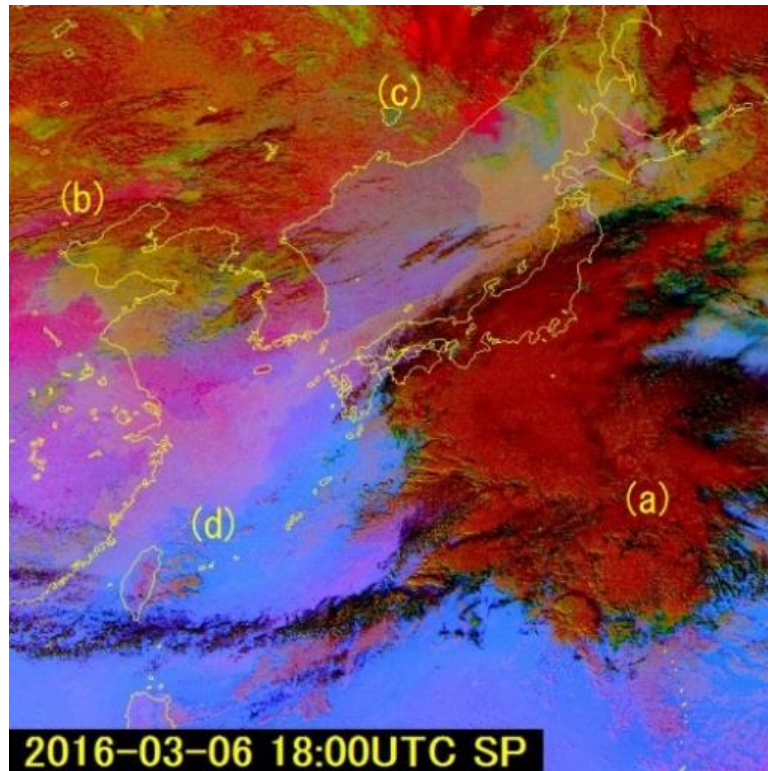


Fig. 1-4-22. Dust RGB composite image for 18:00 UTC on 6 March 2016

(9) Night Microphysics RGB Composite Imagery

The fog and low-cloud area (d) is shown in white with traces of green (Fig. 1-4-23). The cloud area (a) is shown in red with yellow dots, which are particularly prominent in the area reaching the tropopause. The cloud area (b) is clearer than in Dust RGB. Figure 1-4-24 shows a surface weather chart for 12:00 UTC on 6 March 2016.

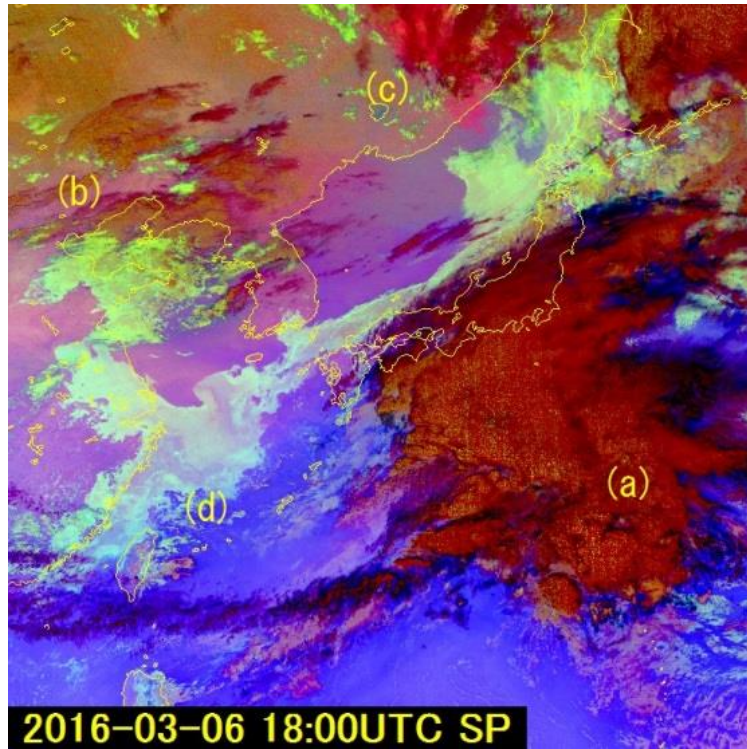


Fig. 1-4-23. Night Microphysics RGB composite image for 18:00 UTC on 6 March 2016

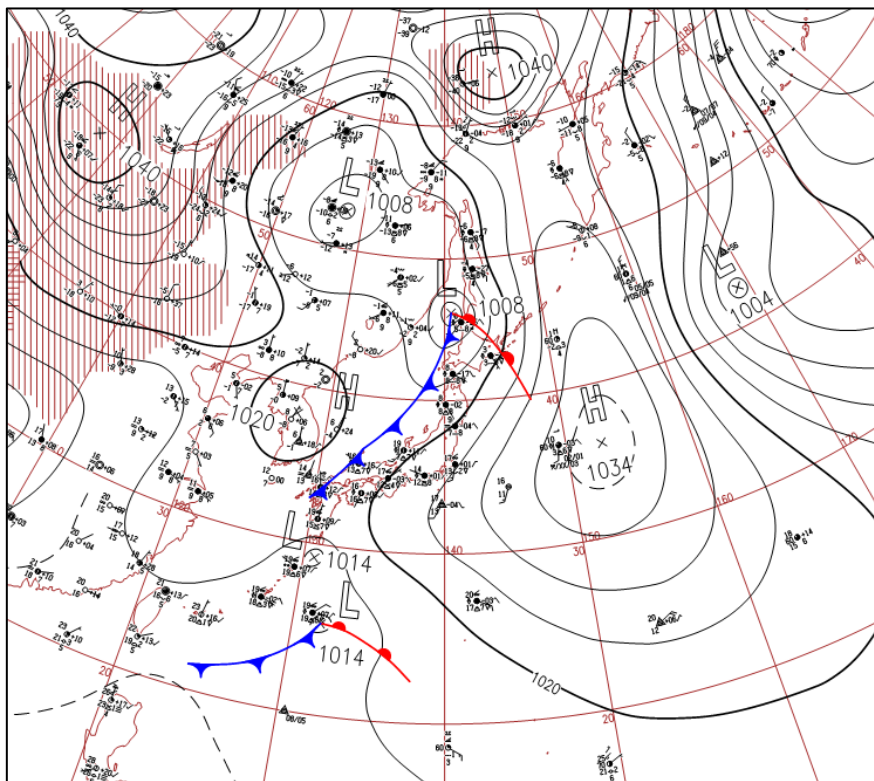


Fig. 1-4-24. Weather chart prompt report for 12:00 UTC on 6 March 2016